Cumulants of event-by-event mean p_{T} distribution in Pb–Pb and pp collisions at LHC energy

A *thesis* Submitted
in Partial Fulfilment of the Requirements
for the Degree of

MASTER OF SCIENCE

by

ARANYA GIRI

with the supervision of

Prof. Bedangadas Mohanty

to the

School of Physical Sciences
National Institute of Science Education and Research
Bhubaneswar

Date : 12-07-2021

In the memory

of my

grandparents

DECLARATION

I hereby declare that I am the sole author of this thesis in partial fulfillment of the requirements for a postgraduate degree from National Institute of Science Education and Research (NISER). I authorize NISER to lend this thesis to other institutions or individuals for the purpose of scholarly research.

Aranya Giri
Date : 12-07-2021

The thesis work reported in the thesis entitled *Cumulants of event-by-event mean p_T distribution in Pb–Pb and pp collisions at LHC energy* was carried out under my supervision, in the school of physical sciences at NISER, Bhubaneswar, India.

Prof. Bedangadas Mohanty
School of Physical Sciences
NISER - Bhubaneswar
Date : 12-07-2021

ACKNOWLEDGEMENTS

My sincere gratitude goes out to *Prof. Bedangadas Mohanty*, my supervisor. His exemplary understanding of the subject and pragmatic ideas helped to comprehend the obtained results and experimental progress of the project. It was never possible for me to go through every basics without his insightful questions during lab presentations. His patience, motivation and immense knowledge have a pivotal role in my academic and professional development. I cannot thank him enough for giving me an opportunity to work with and learn from him.

I am extremely thankful to *Dr. Ranbir Singh* for his guidance which helped me to progress in my project smoothly. I am greatly thankful to him for patiently discussing the problems over phone calls during the COVID-19 period.

Mr. Dukhishyam Mallick help during the project is incomparable. I am thankful to him for reviewing all my results , discussing them patiently, questioning about the progress and keeping me on track every time towards the project. I will always be thankful for his immense support. I am thankful to *Mr. Ashish Panda, Ms. Swati Saha, Mr. Prottoy Das, Mr. Debasish Mallick* for their discussion and expertise regarding my project. I am also thankful to *Dr. Varchaswi Kahsyap, Mr. Vijay Janardhan Iyer, Ms. Mouli Choudury, Mr. Samir Banik* for their support.

Thanks to all my friends at NISER for their companionship and support.

Thanks to *Mr. Rajeev Ranjan Shaw* and *Mr. Gautam Shaw* for their support and teaching during my early academic days. Without their help my interest towards science mostly in physics would not have been possible.

Finally, I would like to thank my dearest parents *Mr. Badal Giri* and *Mrs. Shipra Giri* for their immense support, love and teachings.

Aranya Giri

ABSTRACT

In recent years, study of event-by-event (e-by-e) fluctuations in physical observables has been a topic of interest as this may help physicists to understand the properties of hot and dense matter formed in heavy ion collisions at Large Hadron Collider (LHC) and Relativistic Heavy Ion Collider (RHIC) energies [1]. In this thesis, I tried to understand the e-by-e mean transverse momentum $\langle p_{\mathrm{T}} \rangle$ fluctuations in pp and Pb–Pb collisions at $\sqrt{s_{\mathrm{NN}}}$ = 5.02 TeV . The collision data for Pb–Pb system analysed in this thesis has been taken from ALICE experiment at LHC whereas for pp collision, the events are simulated using PYTHIA8 event generator. Fluctuations of any distributed quantity is encoded in its higher order cumulants. For our analysis, cumulants, C_1, C_2, C_3 and C_4 of e-by-e $\langle p_{\mathrm{T}} \rangle$ distribution for different centrality classes has been compared with gamma distribution, a baseline for statistical fluctuations [2]. Before the comparison, the detector efficiency correction in Pb–Pb collision data is carried out by unfolding and ratio method. Both the method requires the Monte Carlo (MC) data (containing the detector effects) from the experiment. The presence of low MC statistics makes the results skeptical.

PYTHIA8 contains two important phenomenological models for particle production, Color Reconnection and Rope Hydronization. The effect of these two different physics in the models on the cumulants of e-by-e $\langle p_T \rangle$ distribution is also studied.

Contents

List of Figures

Chapter 1

Introduction

Theoretical predictions and experimental observation by thousands of physicists since early 20^{th} century have given us a remarkable understanding to the fundamental structure of matter. The surrounding we see is made of fundamental particles and, the particles are governed by four fundamental forces as seen in fig. (1.2). These elementary particles and their governing force (except gravitational) are explained by the Standard Model [3].

1.1 The standard model of particle physics

Over time and through many experiments, the Standard Model as shown in the fig. (1.1) has become established as a well tested physics theory [4]. It is one of the most important achievement for particle physicist till now. According to the model, the elementary particles can be categorized into six quarks, six leptons, four gauge bosons and the recently discovered Higgs boson. The six quarks are paired into three generations :

- 1st Generation : up (u) and down (d)
- 2nd Generation : charm (c) and strange (s)
- 3rd Generation : top (t) and bottom (b)

and the leptons are also arranged into three generations:

- 1st Generation : electron (e^-) and electron-neutrino (ν_e)
- 2nd Generation : muon (μ^-) and muon-neutrino (ν_μ)
- 3rd Generation : tao (τ^-) and tao-neutrino (ν_τ)

Each of the quarks and leptons also have their corresponding antiparticles with opposite charge.

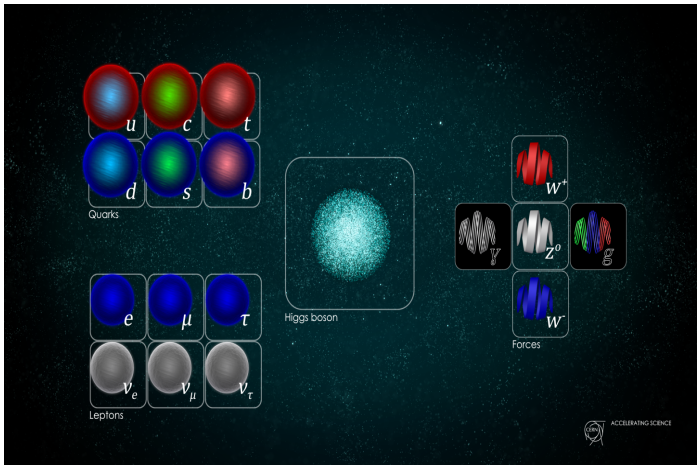

Figure 1.1: Fundamental particles of the Standard Model of particle physics

Each fundamental force acts differently via mediating their respective gauge bosons. Few features of these interactions are as follows :

- The strong interaction, as the name suggests, is the strongest of all four fundamental interactions. It is only effective only at the level of subatomic particles. The interaction is mediated by exchange of gauge boson, *gluon*.
- The weak interaction is also only effective in the subatomic level. This interaction is responsible for slow decay of unstable subatomic level particles. This interaction is mediated by exchange of heavier gauge bosons, *W* and *Z bosons*
- The electromagnetic interaction occurs between every charged particles and is mediated by exchange of *photons*.

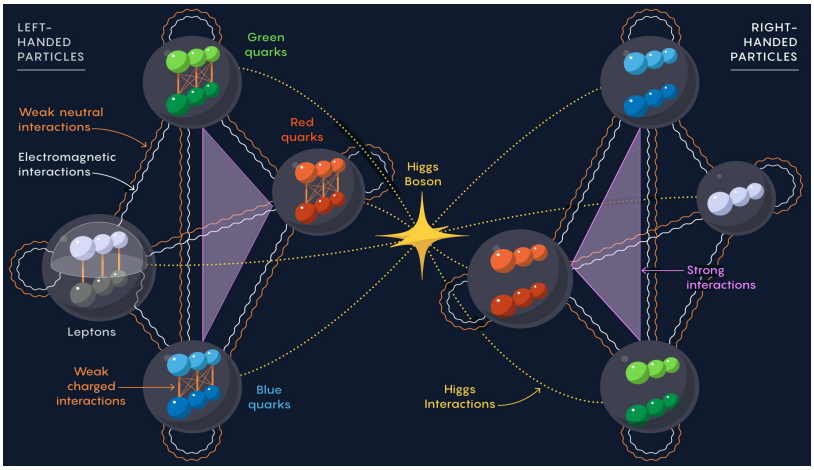

Figure 1.2: A schematic representation of fundamental forces of standard model [4]

1.2 Nature of strong interaction

The theory of strong interaction is described by Quantum Chromodynamics (QCD). The fundamental particles in QCD theory are quarks, anti-quarks and gluons. The strong force between these particles is mediated by the exchange of gluons. Gluons is a boson, and quarks anti-quarks are fermions. Quark (anti-quark) carry *color (anti-color)* charge and gluons carry pair of color anti-color charge. The interaction potential between quark anti-quark pair is approximately stated as

$$V = -\frac{\alpha_s}{r} + \kappa r \tag{1.1}$$

here , α_s is the strong coupling constant and κ is the colour string tension. The strong coupling constant is given by

$$\alpha_s(Q^2) = \frac{12\pi}{33 - 2n_f} \frac{1}{\ln\left(\frac{Q^2}{\lambda^2_{QCD}}\right)} \tag{1.2}$$

where Q^2 is the momentum transfer, n_f is the number of quark flavors and λ_{QCD} is the scale parameter. The coupling constant increases as the distance between the quarks increases thus making them inseparable. This property is known as quark confinement. It is responsible for binding quarks inside the hadrons. The quark anti-quark pair bind together to form a meson, while three quarks bind together to form a baryon. If the distance between the

quarks is small, momentum transfer "Q" between them is large, then the coupling constant α_s becomes small and the quarks behave like a free non-interacting particle. This astonishing property is called *Asymptotic freedom* [5, 6].

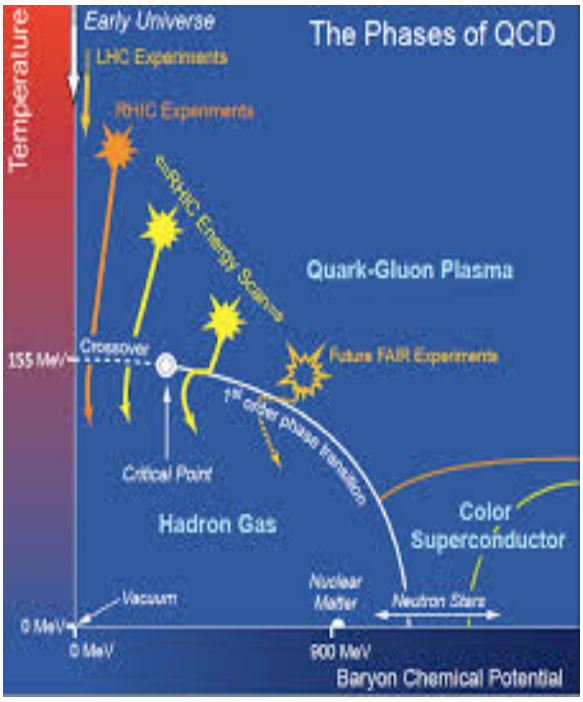

Figure 1.3: A sketch illustrating the experimental exploration of the QCD phase diagram [7]

In hard processes where the momentum transferred during collision is large (α_s is small), QCD calculations can be done perturbatively while in soft processes (dominant process) it cannot be treated perturbatively (α_s is large). The QCD can be solved non-perturbatively by lattice QCD approach where the calculation is done on a discrete space time lattice. Lattice QCD calculations predicts transition from a confined hadron to a deconfined partonic matter at temperature around 150 MeV [8, 9]. It was believed that high density nuclear matter containing asymptotically free quarks can be created. Such a matter of free quarks and gluons is termed as *Quark Gluon Plasma* (QGP) [10]. The phase diagram of QCD is shown in fig.(1.3).

1.3 Kinematic variables

In high energy heavy ion collision, particles are accelerated to a speed comparable to the speed of light therefore relativistic effects must be taken into consideration when we switch between different frame of references. The light-cone variables, transverse momentum, rapidity and pseudo-rapidity are few observables that have simple Lorentz transformation laws and only depends on momentum and energy of the detected particles.

1.3.1 Mean transverse momentum

Particle detectors which are dedicated to measure the momentum and energy of the produced particles are located on transverse direction (x-y plane) of the beam axis (z-axis). The transverse momentum (p_{T}) is a Lorentz invariant quantity (see appendix A) and is given as,

$$\mathrm{p_T} = \sqrt{\mathrm{p_x^2} + \mathrm{p_y^2}} \tag{1.3}$$

Figure (1.4) shows plots of p_x, p_y, p_z and p_T in Pb–Pb collisions. The small dip in the center of p_x and p_y is due to p_{T} cut ($>$ 0.2 GeV/c) given on data for analysis, as below this detector does is not able measure the momentum correctly. In this thesis we will study event-by-event (e-by-e) mean transverse momentum ($\langle p_{\mathrm{T}} \rangle$), a widely studied observable of an event. The e-by-e $\langle p_{\mathrm{T}} \rangle$ is given as,

$$\langle \mathrm{p_T} \rangle = \frac{1}{\mathrm{N_{track}}} \sum_{\mathrm{i=1}}^{\mathrm{N_{track}}} \mathrm{p_{T_i}} \tag{1.4}$$

Here, index i refers to $\mathrm{i_{th}}$ charge particle in an event and $\mathrm{N_{track}}$ is the total no. of charge particle detected (or produced) in the event, event charge multiplicity. Figure (1.5d) shows e-by-e $\langle p_{\mathrm{T}} \rangle$ distribution in Pb–Pb collisions.

1.3.2 Rapidity

Let us consider a particle resulting from from a collision such that it has four-momentum $\mathbf{p}$ $(\mathrm{p_0}, \mathrm{p_T}, \mathrm{p_z})$, then the *forward light-cone momentum* and *backward light-cone momentum* are given as $\mathrm{p_+} = \mathrm{p_0} + \mathrm{p_z}$ and $\mathrm{p_-} = \mathrm{p_0} - \mathrm{p_z}$ respectively. On Lorentz transformation, these quantities get multiplied by a constant factor (see A.5).

Rapidity (y) of the particle is related to the ratio of p_+ and p_-. Mathematically it is expressed as

$$y = \frac{1}{2}\ln\left(\frac{p_0 + p_z}{p_0 - p_z}\right) \tag{1.5}$$

Lorentz transformation yields simple relation (for derivation see A.5),

$$y' = y - y_\beta \quad \text{here}, y_\beta = \frac{1}{2}\ln\frac{1+\beta}{1-\beta} \tag{1.6}$$

Here, y' is rapidity in frame F' and y in frame F (F' moves with velocity β wrt F).

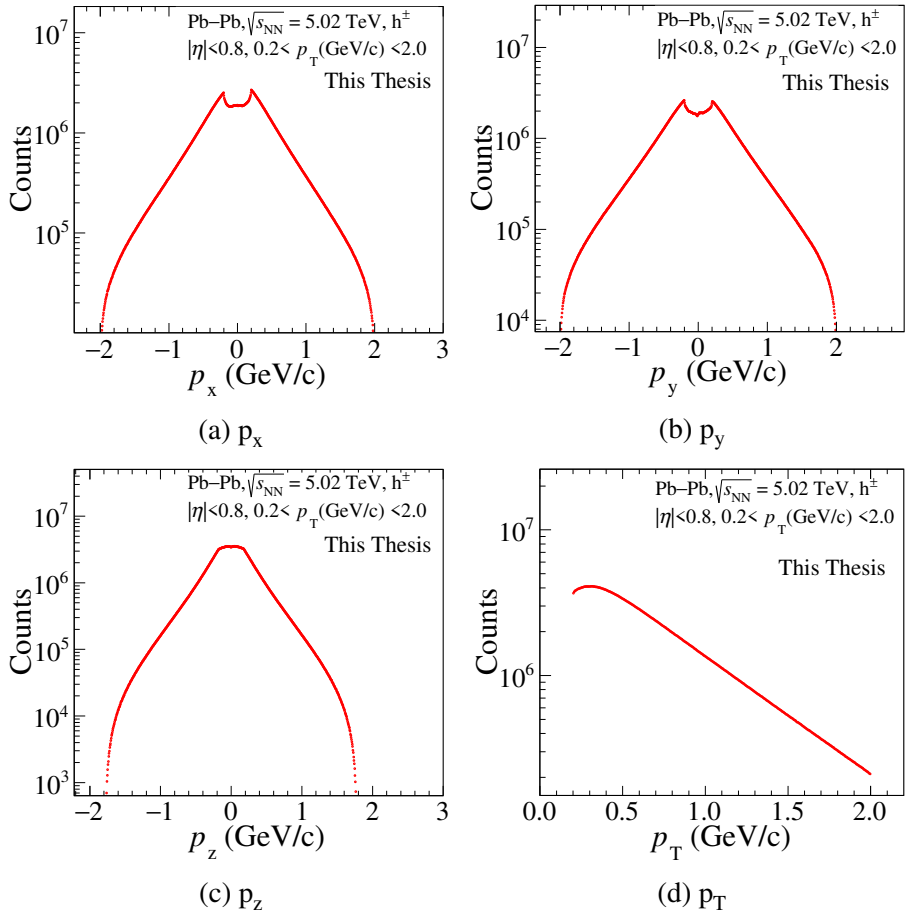

(a) p_x (b) p_y

(c) p_z (d) p_T

Figure 1.4: Few kinematic variables of charge hadrons produced in Pb—Pb collisions. The y-axis represents total count of tracks over all the events.

1.3.3 Pseudorapidity

Pseudorapidity (η) is another kinematics variable which depends only on the azimuthal angle θ by the mathematical relation (1.7). Figure (1.5a) shows a typical pseudorapidity

distribution in Pb–Pb collision, it is almost constant. This has certain advantage that detectors requires only one observable to measure.

$$\eta = -\ln\left(\tan\frac{\theta}{2}\right) \tag{1.7}$$

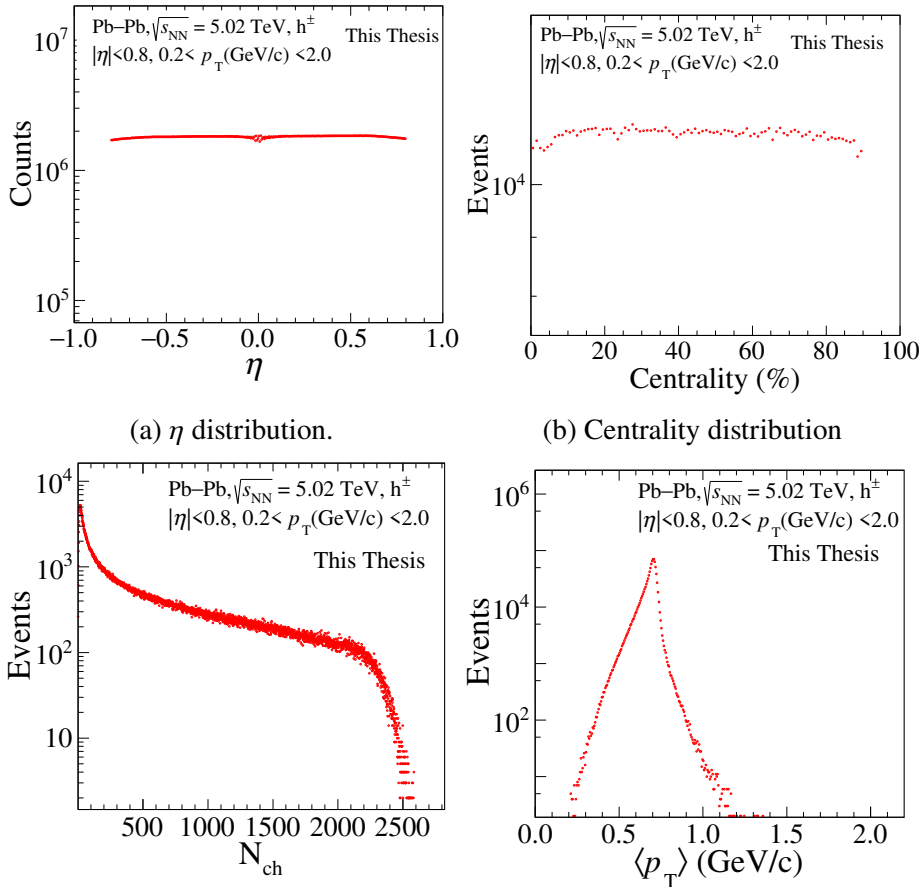

(a) η distribution.

(b) Centrality distribution

(c) Charge multiplicity distribution.

(d) Event-by-event $\langle p_T \rangle$ distribution.

Figure 1.5: Different physical observables in Pb–Pb collisions

There is one more definition of η which depends on $|\vec{p}|$ and p_z and is given by,

$$\eta = \frac{1}{2}\ln\left(\frac{|\vec{p}| + p_z}{|\vec{p}| - p_z}\right) \tag{1.8}$$

In high energy collisions, $p_0 \approx |\vec{p}|$. Therefore rapidity and pseudorapidity are comparable, $\mathbf{y \approx \eta}$.

1.4 Centrality

Centrality is a measure of "how much" a collision is head-on. It is used in heavy-ion collisions to characterize an event. Complete details about the calculation of centrality classes can be found in paper [11, 12]. Here a brief background understanding is presented as in our analysis the centrality of each event is determined by a pre-defined ALIROOT.

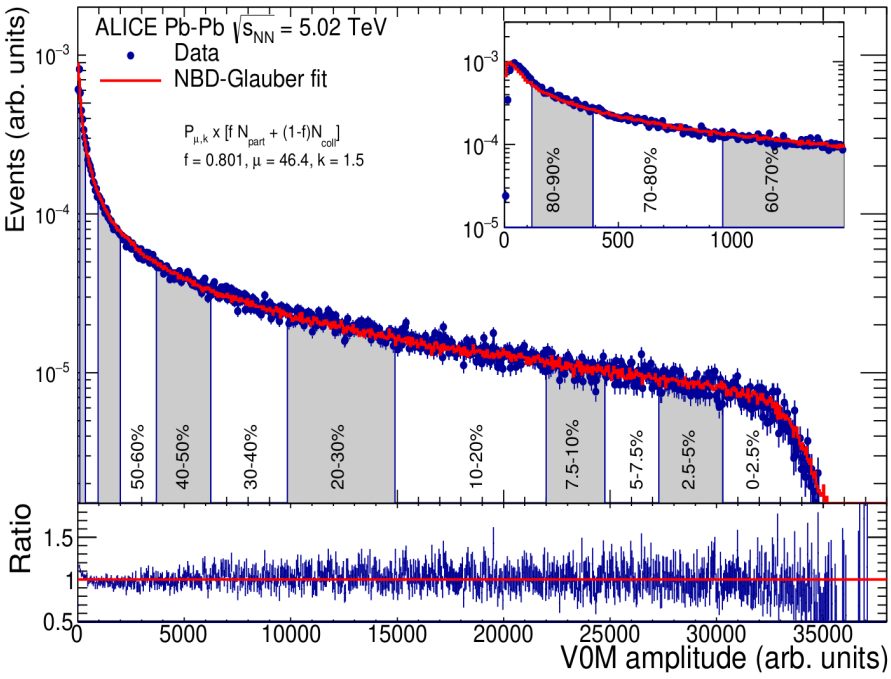

Figure 1.6: Normalised charge multiplicity distribution with NBD-Glauber fit distribution. In the x-axis, the V0M amplitude is directly proportional to charge particles detected in the V0 detectors. The lower panel shows the ratio of experimental and fitted values. The figure is taken from the paper [11]

Centrality classes are constructed by taking into account the whole area under the multiplicity curve and dividing this area accordingly from the right to left such that low centrality values correspond to central collisions and high centrality values to the peripheral collisions. While defining centrality classes we assume that the impact parameter **b** is monotonically related to particle multiplicity(N_{ch}). For collisions with low impact parameter, produced particles (charge, N_{ch}) is low, and also the momentum of these produced particles will be low such that these particle might not be able travel to the detector (V0). This will

lead to underestimation of events with large impact parameter or low N_{ch} and it further leads to incorrect estimation of area under curve as events with low N_{ch} occurs majorly in the experiment. Hence, the experimentally determined charge multiplicity distribution (fig 1.5c) fails to correctly determine centrality classes.

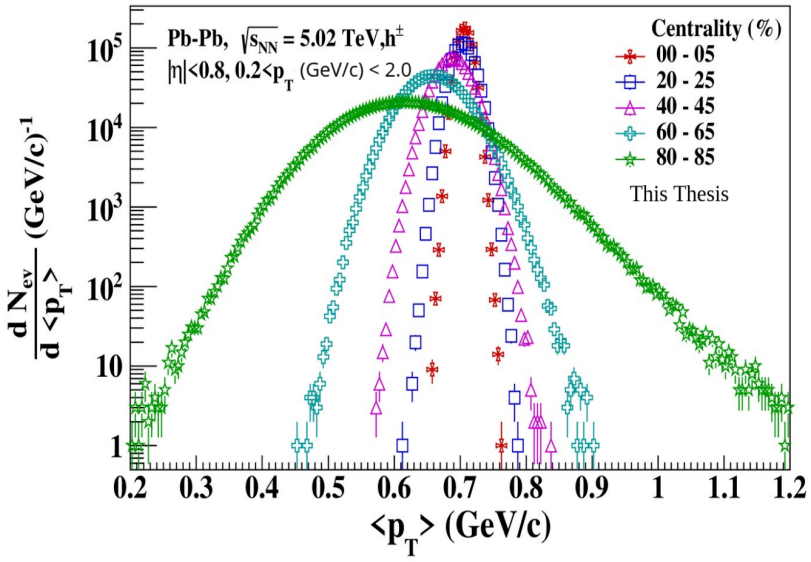

Figure 1.7: Event-by-event $\langle p_T \rangle$ distribution for different centrality classes Pb–Pb collisions.

To correct this discrepancy, a Negative Binomial Distribution-Glauber model fit is done to the data as shown in fig. 1.6 [12]. The fitted distribution is used to calculate the centrality classes for the experimental data. Figure (1.7) shows e-by-e $\langle p_T \rangle$ distribution for five different centrality classes.

1.4.1 Multiplicity Percentile

In proton-proton (pp) collision, multiplicity percentile is used to characterize events, It has the same meaning as centrality in heavy-ion collisions. Head-on collisions imparts Multi-Parton Interactions (MPIs) resulting in large multiplicity. Therefore low multiplicity percentile is defined as most central collision and high multiplicity percentile as peripheral collisions. Thereafter the total area under multiplicity distribution is diced as shown in fig. (1.8). The method used to cut the multiplicity distribution in simulated pp collision is simple due to absence of detector effects. Figure (1.9) shows e-by-e $\langle p_T \rangle$ distribution for

six different multiplicity classes.

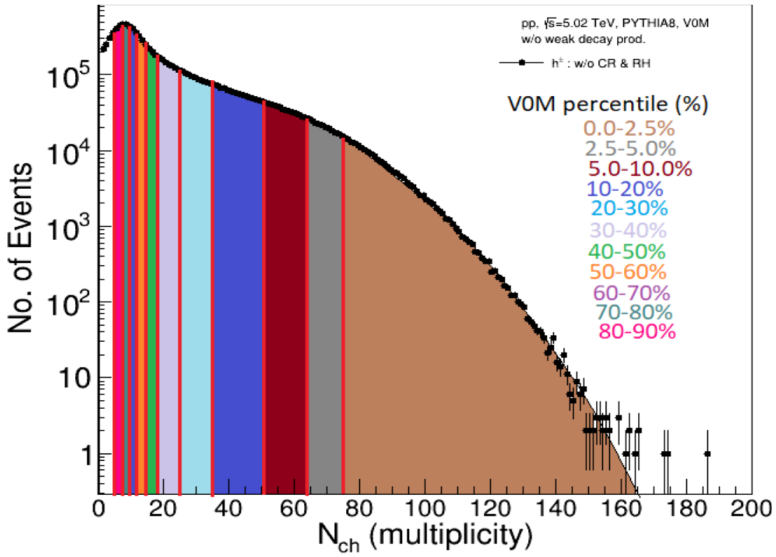

Figure 1.8: Plot shows the multiplicity (V0M when actual data is used) percentile division of the charge multiplicity distribution in pp collisions.

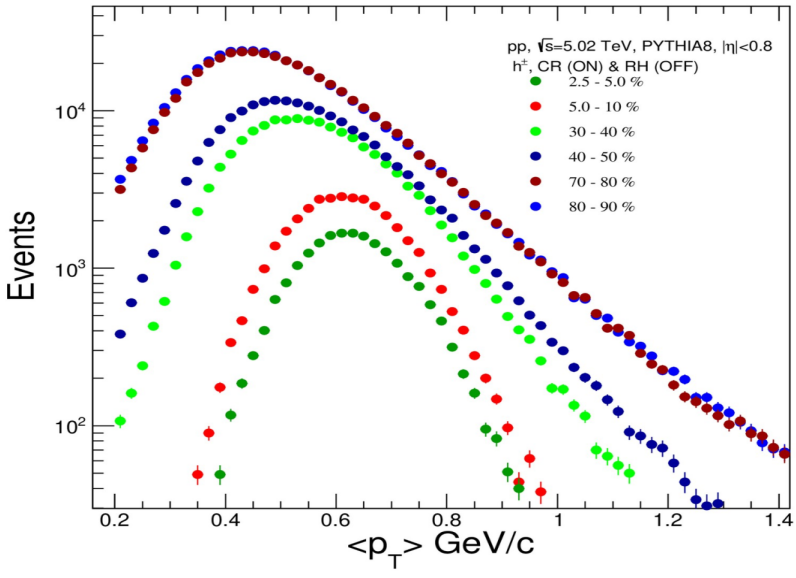

Figure 1.9: Event-by-event $\langle p_{\mathrm{T}} \rangle$ distribution for different multiplicity percentile classes in pp collisions.

1.5 Cumulants of distribution

Cumulants are numbers that quantify shape of a distribution. For a given random variable x,

$$C_1 = \mu_1^{'} \tag{1.9a}$$

$$C_2 = \mu_2 \tag{1.9b}$$

$$C_3 = \mu_3 \tag{1.9c}$$

$$C_4 = \mu_4 - \mu_2^2 \tag{1.9d}$$

Here the raw moment $\mu_1^{'}$ is the mean of the distribution of x and given as,

$$\mu_1^{'} = \sum_{i=1}^{N} x \tag{1.10}$$

and the central moment μ_r is calculated as,

$$\mu_r = \sum_{i=1}^{N} (x - \mu_1)^r \tag{1.11}$$

In our analysis, x is event-by-event mean transverse momentum $\langle p_T \rangle$ and N is N_{event}, the total number of events. The error on cumulants are calculated using delta-theorem and are given as,

$$\mathrm{Var}(C_1) = \frac{\mu_2}{n} \tag{1.12}$$

$$\mathrm{Var}(C_2) = \frac{1}{n}\left[\mu_4 - \mu_2^2\right] \tag{1.13}$$

$$\mathrm{Var}(C_3) = \frac{1}{n}\left[\ \mu_6 - \mu_3^2 + 9\mu_2^3 - 6\mu_4\mu_2\ \right] \tag{1.14}$$

$$\mathrm{Var}(C_4) = \frac{1}{n}\left[\ \mu_8 - 12\mu_6\mu_2 - 8\mu_5\mu_3 - \mu_4^2 + 48\mu_4\mu_2^2 + 64\mu_3^2\mu_2 - 36\mu_2^4\ \right] \tag{1.15}$$

A complete calculation is provided in appendix E.

1.6 Motivation for the thesis

The main aim of ALICE experiment at CERN is to study the properties of QGP formed during heavy-ion collisions. To probe the properties of QGP, many authors studied the event-by-event (e-by-e) fluctuations of physical quantities such as charge multiplicity, photon multiplicity, mean transverse momentum and energy. Event-by-event fluctuations are of two kind : Statistical and Dynamical. Dynamical fluctuations arise from different sources of correlations among the final-state particles, such as jets, resonance decays or quantum correlations [13] whereas the statistical fluctuations arises due to limited acceptance of the detectors, finite particle multiplicity, fluctuations in the number of primary collisions, impact parameter fluctuations, or effects of re-scattering of secondaries [14, 1]. To probe the dynamical fluctuation (if present) which might be associated to some new physics, it is necessary that we first understand the expected statistical fluctuation. If the particles are emitted independently, the fluctuations will be purely statistical and its baseline for e-by-e mean transverse momentum ($\langle p_{\mathrm{T}} \rangle$) distribution will be gamma distribution [2]. In this thesis, I have compared the e-by-e $\langle p_{\mathrm{T}} \rangle$ distribution for different centrality classes with be gamma distribution to check whether the observed fluctuations is purely statistical as was earlier found in central collisions for Pb–Pb system at $\sqrt{s_{\mathrm{NN}}}$ = 158 GeV [2].

Fluctuations study in small collision systems like proton-proton act as a model independent baseline to search for non-trivial fluctuations in heavy-ion collisions [13]. Therefore the same analysis is performed in pp system (in PYTHIA model) to understand the difference in fluctuations that we observe in Pb–Pb system.

Chapter 2

Pythia8 simulation for pp collision

PYTHIA is a computer simulation program which virtually collides elementary particles like $e^-, e^+, p, \bar{p}$ and mimics the high energy particle accelerator experiments. The mimicking process like for initial and final state radiation, beam remnants, multiple parton interactions, hadronization and particle decays is based on several coherent physics models. **PYTHIA8** is the newest version of this event generator and it is written in C++ platform [15].

2.1 hadronization

Hadronization of produced quarks (anti-quark) and gluons into observed hadron lies in the non-perturbative QCD regime and hence a complete theoretical understanding is still missing. PYTHIA8 implements Lund string fragmentation model for hadronization as seen in fig. (2.1). This model incorporates color strings between partons which then later on fragments successively into final state hadrons.

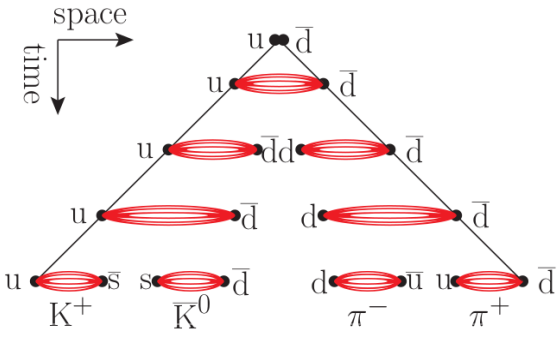

Figure 2.1: A schematic diagram of string fragmentation model of hadronization [16]

The the model also has many limitations like ,

1. It is unable to explain the observed flow like patterns or in simple words the increase in transverse momentum of the particle with event multiplicity[17].

2. Mechanism underestimates production of strange and baryon particles in proton-proton collision [18].

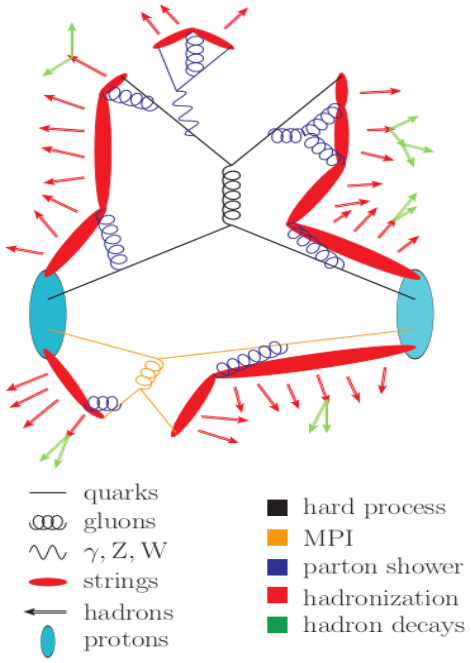

Figure 2.2: A phenomenological diagram of proton-proton collision in the event generators perspective. [16]

2.1.1 Color Reconnection

A proton-proton collision with high multiplicity is accompanied by multiple parton-parton interactions (MPI) and each parton is classified by the MPI system they belongs to or to say from which parton-parton collision they were produced. The high multiplicity events are naturally accompanied by high parton density and this phenomena then favour more than one pair of quark and anti-quarks in the vicinity of each other.

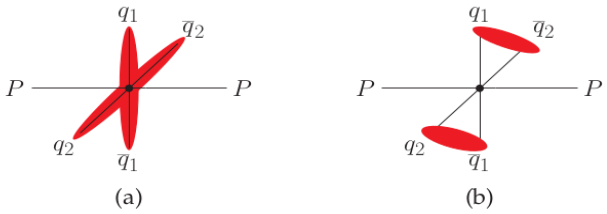

Figure 2.3: Examples of two closely spaced dipoles (quark & anti-quark pair) formed from same proton-proton collision but different MPI system. They can form two different configuration (a) or (b).The image is reproduced from reference [16]

As from the fig.(2.2) we know that partons are color connected (strings are present) to their beam remnants and there is already a inherited strings connections present between partons of each MPI system. In default these inherited strings breaks successively into hadron. **Color Reconnection** is a model which decides whether the strings between two dipoles of MPI sytems can switch or not in order to reduce their potential energy or their string length (given by λ measure). This problem can be visualized with the sample fig. (2.4) presented below.

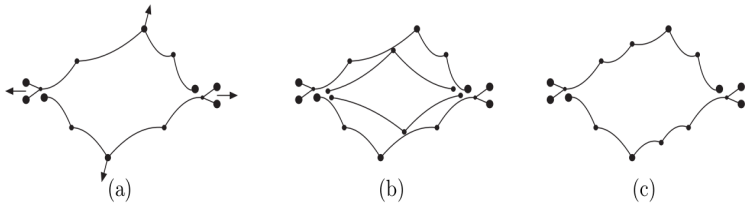

Figure 2.4: An example of hard parton-parton sub-collision. (a) The outgoing partons (top and bottom dots) as colour connected to the projectile and target remnants (left and right dots). Initial state radiation may give extra gluon kinks (small dots in between strings) (b) A second hard scattering would give two new strings (from top & bottom to left & right) connected to the remnants. (c) The partons are colour reconnected, so that the total string length becomes as short as possible. The image is reproduced from reference [19]

2.1.2 Rope hadronization

High multiplicity events in proton-proton collision is accompanied with MPIs and hence high density of dipoles. This leads to large number of strings occupying the same transverse area ($\sim$ 1fm^2). Rope Hydronization (RH) model takes into account the interaction of these overlapping strings through two distinctive way :

1. By allowing the overlapping strings to push/shove each other in the respective outward direction as seen in fig. (2.5).

2. The color charges and/or the “gluon kinks" at the end points of the overlapped strings can coherently form a rope, having colored multiplet and larger effective string tension. This effect is also known as **flavour ropes** as it has considerable effects on the flavour composition of final state hadron composition.

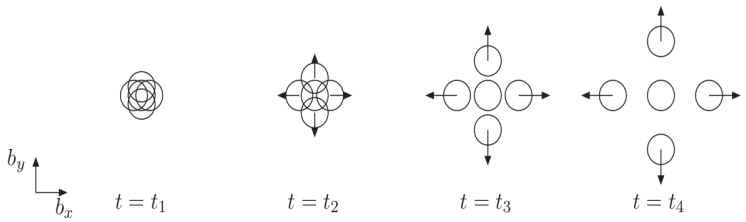

Figure 2.5: A schematic diagram showing the overlapped dipoles (quark & anti-quark pair) in impact parameter ($\vec{b}$) space. The image is reproduced from reference [20]

2.2 Event and Track selection for analysis

In this project, the pp collision events are generated in PYTHIA8(vs .235) with the selection criteria for events depending on the ALICE detector.

- Collision energy : $\sqrt{s}$ = 5.02 TeV
- No. of events : 10 Million
- Hadrons ($h^{\pm}$) : $p^{\pm}$, $\pi^{\pm}$ and $K^{\pm}$
- particle must not be produced via weak decay.
- produced particle should be product of collision only.
- Multiplicity Distribution :
  - η range (ALICE V0M detector [21]) : $-3.1 < \eta < -1.7$ (V0C) or $2.8 < \eta < 5.1$ (V0A)
- event-by-event $\langle p_T \rangle$ distribution :
  - η range (ALICE TPC detector [21]) : $|\eta| < 0.8$
  - p_T cut : $0.2 < p_T < 2.0$

The particles generated virtually in the event generator are detected symmetrically in η and ϕ range but to mimic the detector acceptance range, the above selection criteria are followed then the generated events are selected as an observation if and only if there is atleast one particle detected in η range of both V0M and TPC detector [21].

Now, four different configuration of CR and RH model has been used to generate events. These configurations are as follows :

1. CR (ON) and RH (OFF) : CR model without RH model. This is also the default configuration in PYTHIA8.
2. CR (ON) and RH (ON): Both CR and RH model included.
3. CR (OFF) and RH (OFF) : Both the models are excluded.
4. CR (OFF) and RH (ON) : RH model without CR model.

To get a general idea only the default tunes of each models are used i.e, CR is the default MPI based model and RH model has the default tune of shoving and flavour on always.

2.3 Event-by-event $\langle p_T \rangle$ cumulants in pp system

To understand the effect of model configuration charge multiplicity distribution and first four cumulants of event-by-event $\langle p_T \rangle$ distributions are compared with respect to each other.

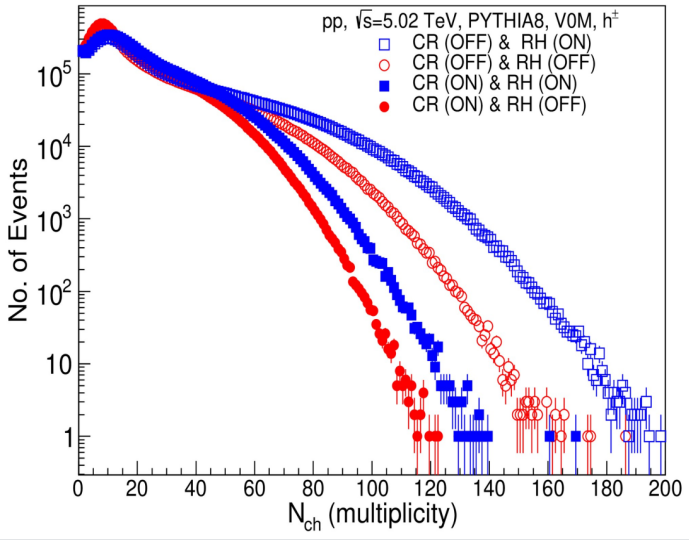

Figure 2.6: Charge multiplicity distribution for various model configuration

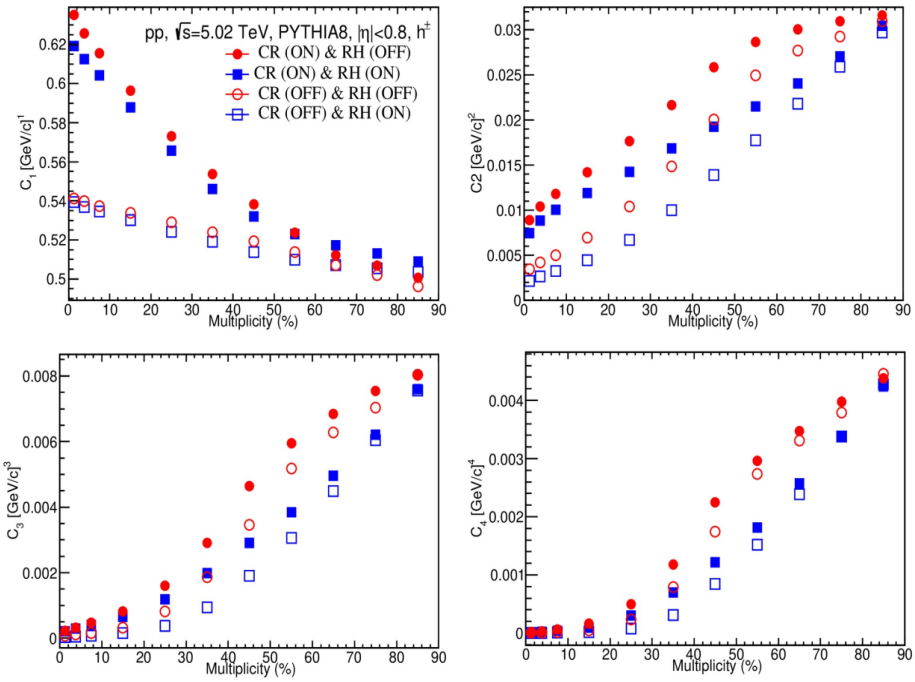

Figure 2.7: Variation of cumulants of event-by-event $\langle p_{\mathrm{T}} \rangle$ with multiplicity percentile for various model configuration. The y-axis represent respective cumulant and x-axis represent multiplicity percentile classes.

1. For charge multiplicity distribution,

   - Effect of each model is prominently seen in lower ($N_{ch} \lesssim 20$) and higher multiplicity ($N_{ch} \gtrsim 50$) events as seen in fig. (2.6). After reviewing each model it is well understood that both the models will greatly effect the event generation by increasing or decreasing events with high multiplicity and as the no. of event generated is same in all configuration. If events with high multiplicity are enhanced or suppressed, the lower multiplicity events gets suppressed or enhanced respectively.
   - Keeping CR model either ON or OFF : RH enhances events with higher multiplicity.
   - Keeping RH model either OFF or ON : CR suppresses events with higher multiplicity.
   - On compared to default ; applying RH model or removing CR model, events

with higher multiplicity are enhanced.

2. And for event-by-event $\langle p_T \rangle$ distribution cumulants,

   - CR increases the C_1 and it increases monotonously as centrality decreases as seen in fig. (2.7). CR flips the strings between a low p_T dipole of one MPI system and a high p_T dipole of another MPI system (with a probability that is inversely proportional to the square of p_T). The p_T of the newly formed dipoles is more than the former one and hence there is enhancement of mean, C_1. Decreasing centrality means decreasing the impact parameter of the collisions. Lower centrality results from head-on collision in which MPIs occurs and it also increases with decreasing centrality. And higher MPIs mean, larger dipole density and the CR effect is seen much more.
   - CR also increases the C_2 and it decreases monotonously with CR as centrality decreases. CR works iteratively, taking the lowest p_T dipole and tries to connect with successive higher p_T dipole with probability remaining the same. This results in increase in variation (C_2) of dipole's p_T compared to the case where CR effect is not seen.
   - C_1 and C_2 are slightly larger with RH for large centrality ($\gtrsim 80\%$).
   - C_3 and C_4 increases with increasing centrality. Comparison between each model is complex but the behaviour is different from C_1 and C_2 as for lower and higher centrality each configuration asymptotically becomes same.

Chapter 3

The Experimental Setup

A particle accelerator pushes charge particles like protons, electrons or ions at a speed which is close to the speed of light. These accelerated particles are then smashed either onto a fixed target or against particles accelerating in opposite direction. Study of these collisions help us to unfold the world of the infinitely small.

The European Council for Nuclear Research, CERN (in French Conseil Européen pour la Recherche Nucléaire) holds the largest particle physics laboratory in the world. The main attraction of CERN is the Large Hadron Collider (LHC) which till date remains the world's largest and most powerful particle accelerator dedicated to study fundamental physics.

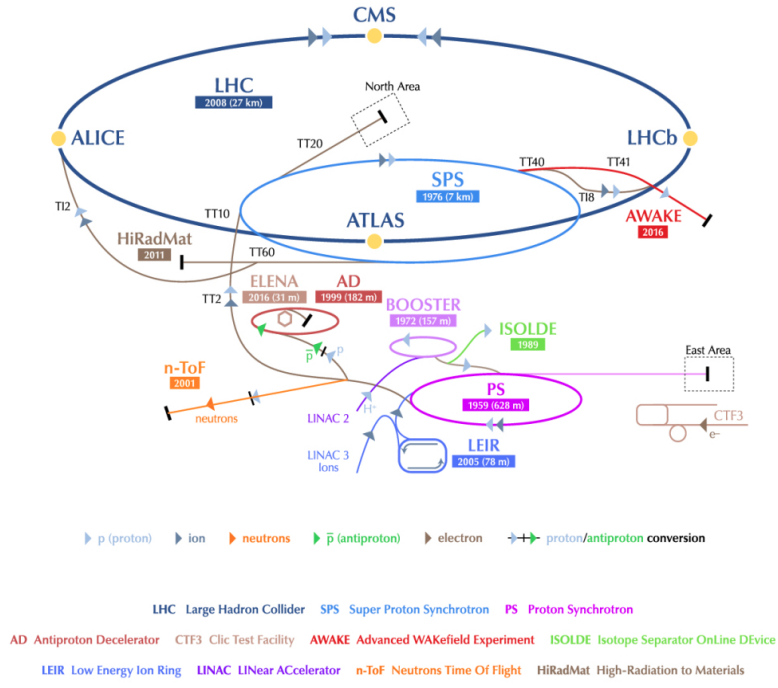

Figure 3.1: A pictorial representation of accelerator complex at CERN. The largest oval shaped ring is the LHC accelerator. The four yellow markers at the LHC ring are the location of four major experiments, ALICE, ATLAS, CMS and LHCb [22].

3.1 The Large Hadron Collider

On 10th September 2008, LHC was added to the CERN accelerator complex. It lies underground at a depth of 50 - 150 m in a 27 km long tunnel across the Switzerland and France border. It is a circular structure of superconducting magnets, and is divided into eight octants. Each octant are 2.45 km long arcs containing 154 dipole magnets. The LHC is designed to collide pair of heavy-ions with maximum center of mass energy of 5.5 TeV per nucleon. The experimental discussion will be mainly on Pb–Pb system which is used in my analysis; apart from this, other colliding system includes pp and p-Pb.

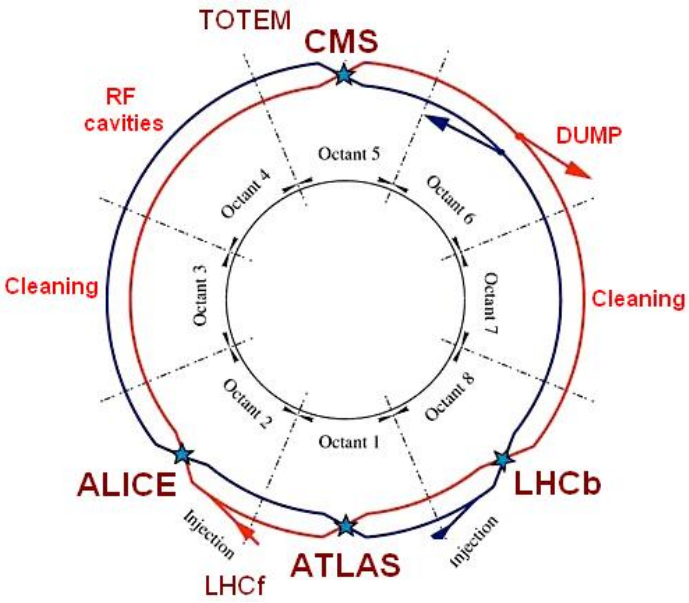

Figure 3.2: The schematic diagram shows different components of Large Hadron Collider (LHC) [23]

At first, pure lead (Pb-208) sample is heated to about 500 ^{o}C to get vapours of Pb atoms. In the the initial stage only few electrons are removed from the atoms using an electric filed. The partially ionised atoms first travels through a linear accelerator called LINAC 3. After attaining an energy of 4.5 MeV per nucleon at LINAC3 few more electrons removed. The ions are then collected and accelerated to an energy of 72 MeV per nucleon in the Low Energy Ion Ring, or LEIR. The beam is then accelerated to an energy of 5.9 GeV per nucleon at Proton Synchrotron (PS), having a circumference of 628 m. Thereafter the beam

is further accelerated to a much higher energy of 177 GeV per nucleon at the Super Proton Synchrotron (SPS) which has a circumference of 7 km. After this step-by-step increment of energy, the ions are finally divided into bunches travelling in opposite direction of the LHC main ring. At LHC, the ions are accelerated to the desired energies before collision.

The pictorial representation of the CERN accelerator complex is shown in figure 3.2.

- At octant 2 and 8, the particles are injected to the LHC ring.
- At the octant 4, the beam is accelerated by Radio Frequency (RF) system.
- At octant 3 and 7, particles having large spatial spread from the bunch center are removed by the collimation system.
- The four major detectors are located at octant 1, 2, 5 and 8. At these points, oppositely accelerated beams collides.
- At octant 6, the beam is removed from the LHC ring by the beam dumping system.

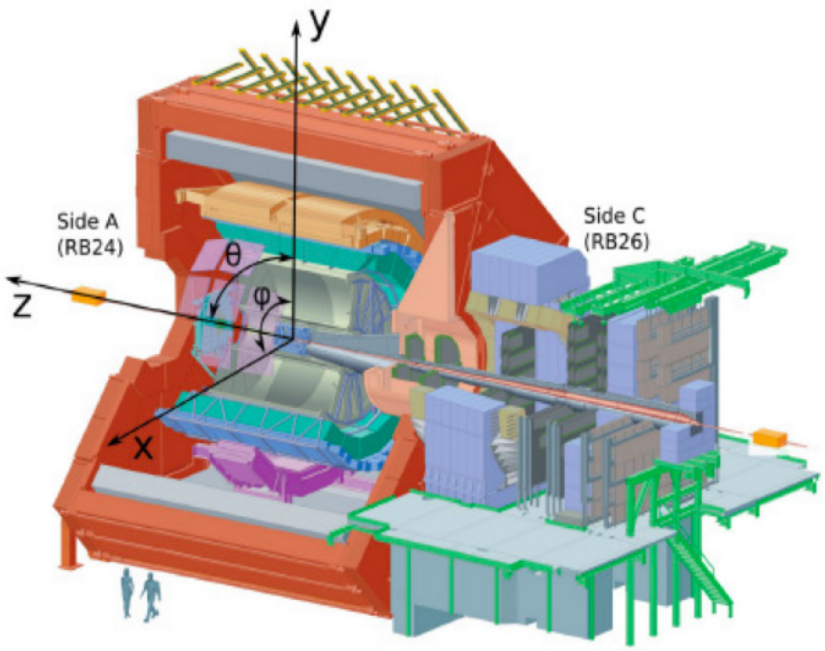

Figure 3.3: The schematic diagram shows the Cartesian coordinate system used at ALICE. Image taken from [24]

The co-ordinate system assigned to the detector is shown in fig. 3.3. Conventionally, the interaction point (IP) is chosen as origin (0, 0, 0); Z-axis is along the beam direction; X-axis lies on the horizontal plane of detector and +X-axis point towards the LHC center; +Y-axis points upward and is perpendicular to the Z-axis & X-axis. Cylindrical coordinate system is often more useful seeing the shape of the detector. For an observer standing at - Z-axis and looking towards the IP. The azimuthal angle, ϕ runs clockwise from +X-axis covering an total angle of 2π whereas the polar angle, θ runs from -Z to +Z direction covering an angle of π.

There are six experiments running in parallel at the LHC.

1. ALICE (A Large Ion Collider Experiment)
2. ATLAS (A Toroidal LHC ApparatuS)
3. CMS (Compact Muon Solenoid)
4. LHCb (LHC-beauty)
5. LHCf (LHC-forward)
6. TOTEM (TOTal Elastic and diffractive cross section Measurement)

The thesis work is based on data taken from ALICE experiment. A brief details of ALICE experiment is described in the following section.

3.2 ALICE at the LHC

The main motivation of ALICE experiment is to understand the formation and evolution of highly dense nuclear matter formed during the collision of heavy-ions. The detector is located at the second octant of the LHC ring as seen in fig. 3.2. It weighs around 10 thousand tonnes and has a dimension of $26(length) \times 16(height) \times 16(width)$ m^3. It is installed within a magnet of maximum strength 0.5 Tesla. The whole detector is categorised in three components; Central Barrel Detectors (CBDs), a Muon Spectrometer and Forward Detectors.

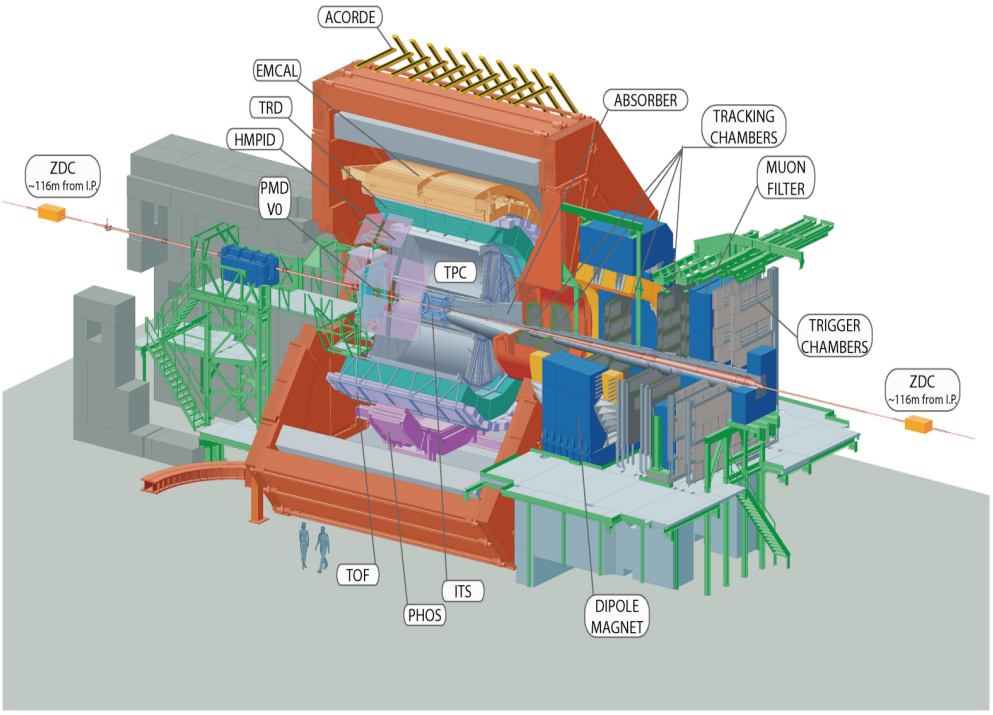

Figure 3.4: The schematic diagram shows the location of different detector at ALICE. Image taken from [24]

3.2.1 Central Barrel Detectors

The Central Barrel Detectors (CBDs) consists of 7 components :

1. Inner Tracking System (ITS)
2. Time Projection Chamber (TPC)
3. Transition Radiation Chamber (TRD)
4. Time Of Flight (TOF) detector
5. High Momentum Particle Identification Detector (HMPID)
6. PHOton Spectrometer(PHOS)
7. Electro-Magnetic CALorimeter (EMCAL)

8. ALICE COsmic Ray DEtector (ACORDE).

The position of each component is shown in figure 3.4. ITS, TPC and TOF are three important detectors related to our data analysis so a brief outline of these detectors are given in the following sub-sections.

3.2.1.1 Inner Tracking System

The beam pipe cylinder is made of beryllium and has a radius of 2.9 cm with a radial thickness of 800 μm. It is surrounded by 6 layers of cylindrical silicon detectors, collectively known as Inner Tracking System (ITS) . The layers further consist of three different categories of detector.

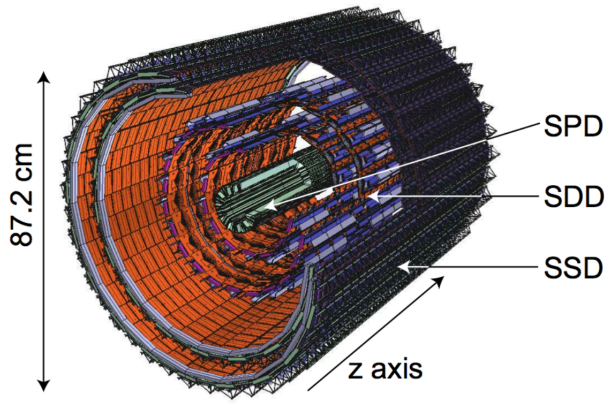

Figure 3.5: A schematic diagram of inner tracking system at ALICE. Image taken from [25]

1. **Silicon Pixel Detector (SPD)** : It is the innermost two layers of ITS. SPD is mainly used for the calculation of primary and secondary vertices and can operate at very high track densities about 50 tracks/cm^3 and in a high radiation environment.

2. **Silicon Drift Detector (SDD)** : They are the two intermediate layers (3rd and 4th) of the ITS. It can give high precision position information (a position resolution of 35 μm) and the information of the energy loss (dE/dx) which can be used for the identification of particles.

3. **Silicon Strip Detector (SSD)** : The SSDs are the outermost layers of the ITS. They play important role in matching the tracks from the ITS to the TPC. It can provide a 2-D

measurement of the track position. In addition it can provide the dE/dx information.

3.2.1.2 Time Projection Chamber

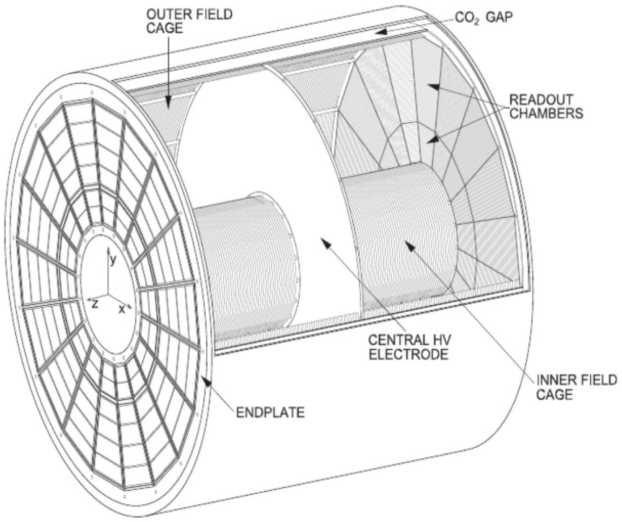

Figure 3.6: Schematic diagram of TPC. Image taken from [23]

The Time Projection Chamber (TPC) is the most important device of the ALICE detector. It is used for tracking and identification of charge particles. The schematic diagram of TPC is shown in fig. 3.6. The TPC is a hollow cylinder surrounding the ITS detector. It has a length of 5 m with an inner and outer radius of approximately 0.8 m and 2.5 m respectively. In between the inner and outer containment vessel, it has a mixture of Ne, CO_2 & N_2 (85.7%, 9.5%&4.8%) gas at atmospheric pressure with a volume of 90 m^3 . The gaseous chamber is divided into two equal zones by a high voltage electrode surface (perpendicular to the axis of TPC). This electrode is a cathode kept at potential of -100 kV, and with the help of voltage dividing network at the surface of inner and outer cylinder, it provides a uniform electric field with strength of 400 V/cm. The electric field lines runs parallel to the beam axis from central cathode to the outer end plates (anode at potential +1.5 kV).

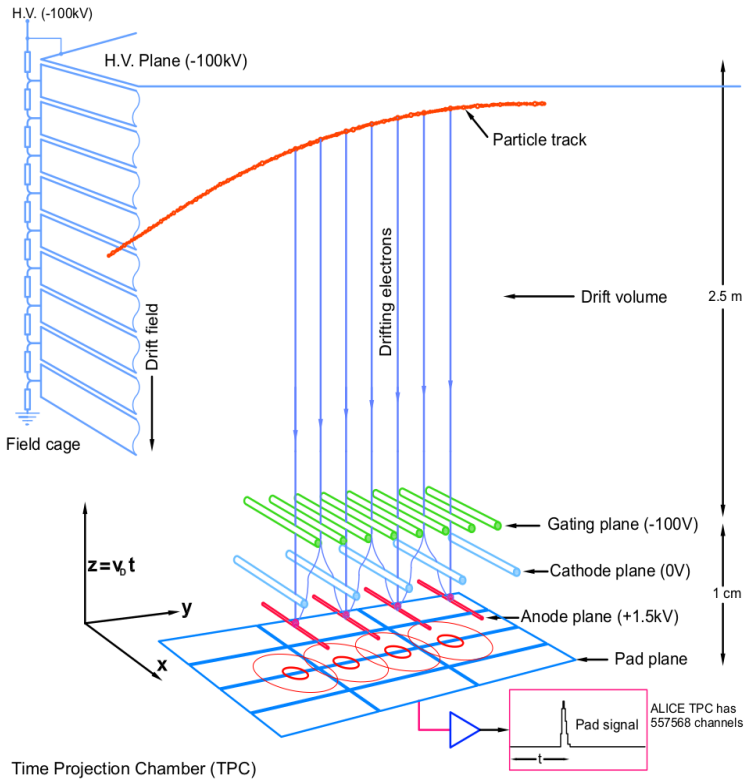

Figure 3.7: Schematic diagram of TPC's working principle. Image taken from [26]

Figure 3.7 shows the working principle of TPC. When a charged particle passes through the active gas volume, it excites and ionizes gas atoms along the trajectory of the track. Ionized free electrons are drifted towards the end plates of the cylinder due to the electric field and the ions are drifted towards the high voltage cathode placed at the centre of the TPC. The drifting of electrons are not affected by the external magnetic field as it is oriented parallel to the electric field. Drifted electrons are amplified by an avalanche process at the end of drift path around the anode wires. The x, y positions of the tracks are reconstructed from the hits on the anode pads at the end plates. The z-coordinates of the tracks are calculated based on the information of drift velocity and arrival time of the drift electrons at the anode plane. The tracks are reconstructed from the 3D space points and the curvature of the track helps in determination of p_{T} of the tracks.

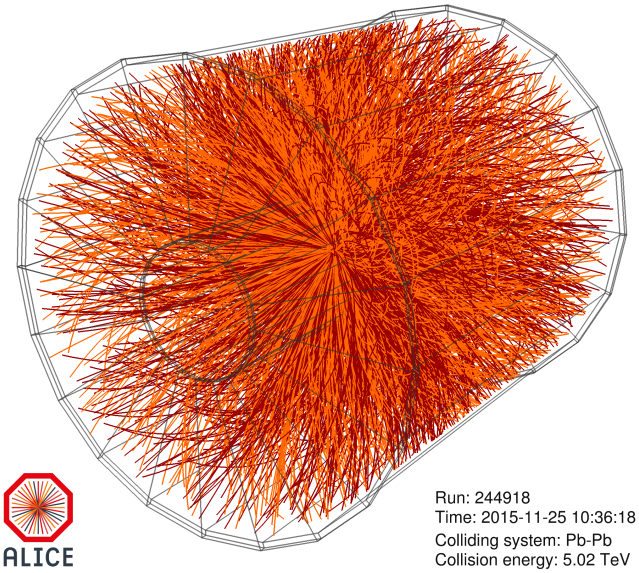

Figure 3.8: The red and orange lines shows the tracks of an actual event recorded by ALICE detector. Image taken from[27].

3.2.1.3 Time of Flight Detector

The TOF detector at ALICE measures the time taken by the particles to reach the detector from the vertex where it was produced and thus helps to measure the speed of the particles. It is based on Multigap Resistive Plate Chambers (MRPCs). Around 1593 MRPCs with active volume of 1.2×0.74 m^2 are arranged on the 18 azimuthal sector. The MRPCs has a double-stack design, it is made of two stacks of 5 gas gaps (250 μm). As the charged particle ionize the gas while transversing the detector, high electric field amplifies the ionization through electron avalanche, which are stopped due to the resistive plates. The total signal is the sum of all the signals from all gaps. It has an ability to detect particles with 99.9 % efficiency with a time resolution of about 85 ps in Pb–Pb collisions. The particles in TOF can also be identified by an Nσcut [24]. TOF detector also identifies the charge particles in the intermediate momentum range.

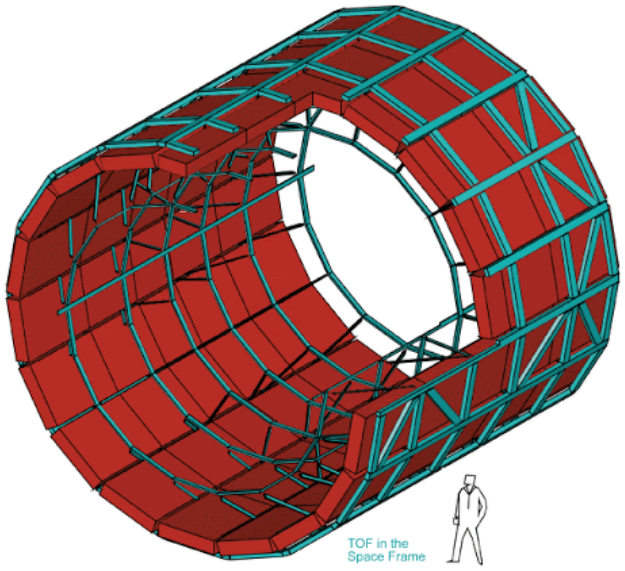

Figure 3.9: A schematic representation of time of flight detector at ALICE. Image taken from [28]

3.2.2 V0 detectors

The two V0 detectors, V0A and V0C are part of ” forward detectors " and are located on either side of beam direction. The V0 detectors are small-angle plastic scintillator detectors situated in the forward directions on both sides of the ALICE collision vertex. They cover full azimuthal angle coverage and the pseudo-rapidity ranges of $2.8 < \eta < 5.1$ for the V0A detector and $-3.7 < \eta < -1.7$ for the V0C detector. Both of the V0 detectors consist of two arrays of 32 scintillator counters. The scintillating light is collected by Photo Multipliers (PMTs) through Wave-Length Shifting (WLS) fibres. Figure shows the position of two V0 detectors in ALICE layout. The V0 detectors are dedicated to provide a minimum bias trigger during the data taking of pp and heavy-ion collisions. They are also used to discriminate the beam-gas interactions by correlating V0A and V0C timing. In addition, V0 detectors are also used to determine the collision centrality in heavy-ion collisions, multiplicity classes in pp collision and event plane by measuring the V0A and V0C amplitudes. Details about the centrality estimation of centrality classes are provided in section.

Chapter 4

Event-by-event $\langle p_{\mathrm{T}} \rangle$ cumulants in Pb–Pb system

4.1 Data-Set

The analysis is carried out with 17 million raw ALICE data and 1 million ALICE MC (HIJING) data fro Pb–Pb collisions at $\sqrt{s_{\mathrm{NN}}}$ = 5.02 TeV. The events were accepted if there is at least one hit in any of V0A, V0C, and SPD, Minimum Bias (MB) trigger (pre-defined in "kINT7"). The centrality of each event is calculated from pre-defined ALIROOT package "V0M estimator". The kinematic cuts for selection of each tracks are

- $0.2 < p_{\mathrm{T}}$ (GeV/c) < 2.0
- $|\eta| < 0.8$

4.2 Cumulants of raw data

The data which we get directly from the experiment is called the raw data. Figure (4.1) shows the higher order cumulants, C_2, C_3 and C_4 of e-by-e $\langle p_{\mathrm{T}} \rangle$ distribution for raw data. Their values are very less for collisions with centrality less than $\sim$ 60%. To see the variation of higher order cumulants with centrality, the y-axis is chosen to be logarithmic.

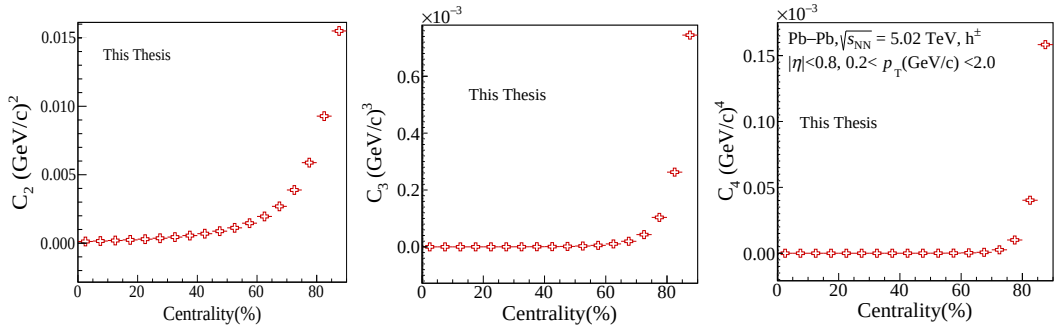

(a) (b) (c)

Figure 4.1: Plot of C_2, C_3 and C_4 of event-by-event $\langle p_{\mathrm{T}} \rangle$ distribution for raw data.

Taking this into consideration, the trend of first four cumulants with centrality can be clearly seen fig. (4.2). C_1 decreases with centrality, and also the rate with which it decreases increases with centrality. In contrast the higher order cumulants increases sharply with centrality.

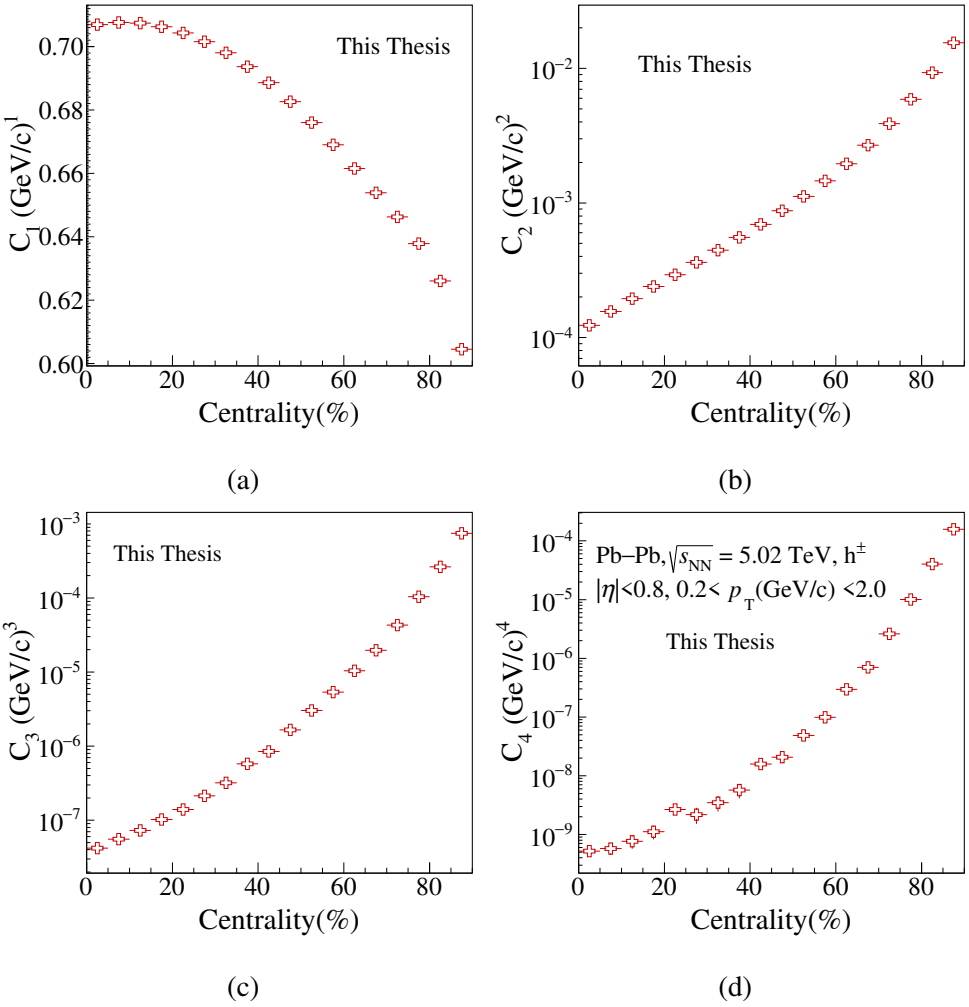

Figure 4.2: Plot shows the cumulants of event-by-event $\langle p_T \rangle$ distribution of raw data. the y-axis of higher order cumulants are in log scale. The vertical line in markers represent statistical error.

The raw data contains detector effects which has to be removed. In the following section we will try to remove the detector effects and get corrected distributions.

4.3 Detector Efficiency Correction

In any experiment, the detector effects or errors are embedded in the measured distribution and thus it differs from the corresponding “true" physical distribution. The aim of physicist is to extract the true distribution by removing these distortions. This is intuitively shown in the fig. (4.3). One of the widely used method to perform this task is Unfolding and Ratio Method.

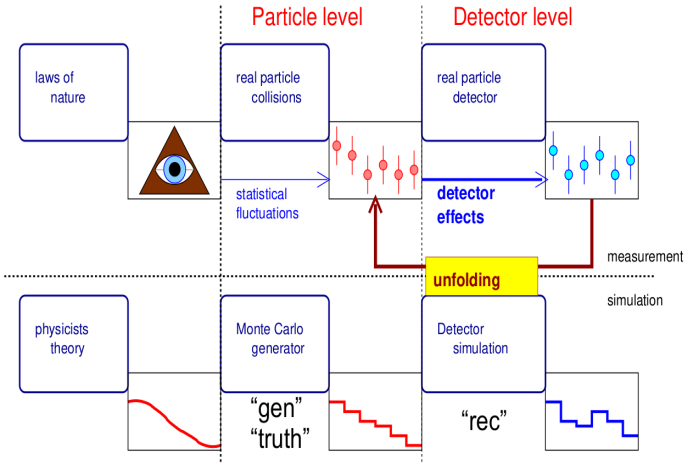

Figure 4.3: A pictorial representation to show different aspects of correcting detector effects[29].

4.3.1 Unfolding

All the measurement effects are encoded in detector **response matrix** which maps the particle level “true" distribution onto the detector level “measured" distribution. If T_i and M_j are the events in bin i and j of true and measured distribution respectively; then the response matrix element R_{ji} is the fraction of events T_i that ends up being measured as M_j. The response matrix is usually created with Monte Carlo simulations taken under same detector conditions during experiment. Unfolding is a process to reproduce the true distribution from the given measured distribution using response matrix [30].

RooUnfold have different pre-coded algorithms to carry out the unfolding process. In this thesis work I have used the **iterative Bayesian unfolding**, widely used by high energy physicist, to remove the event-by-event detector effects. A brief background theory of Bayesian unfolding procedure is provided in the appendix B. The response matrix for this

analysis is created with the generated and reconstructed event-by-event $\langle p_T \rangle$s' of HIJING Monte Carlo simulations from ALICE experiment. The generated (particle level) values are produced from the HIJING model and are then fed in GEANT4 simulation to create the reconstructed (detector-level) values. In the code, the no. of iteration for unfolding is determined by the " χ^2 of change", which reduces as we increase the iterations. This parameter is kept close to 1 for our analysis.

4.3.1.1 Problems with unfolding in Pb–Pb system

The main problem with unfolding in Pb–Pb system is that there is no model which is able to explain the e-by-e $\langle p_T \rangle$ trend with N_{ch} (or centrality). As seen in fig. 4.4 various model like DPMJET, AMPT, Glauber MC and importantly HIJING (used in our analysis) underestimates e-by-e $\langle p_T \rangle$.

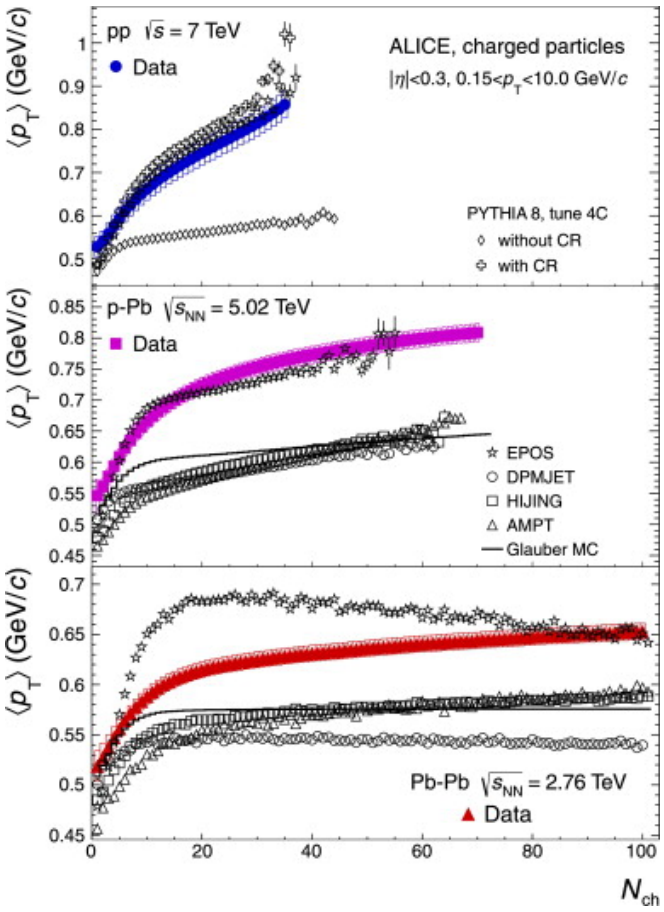

Figure 4.4: Event-by-event $\langle p_T \rangle$ vs charged-particle multiplicity N_{ch} for three different collision systems: proton-proton (upper panel), proton–Pb (middle panel), and Pb–Pb (lower panel). The data results are compared with various model calculations.[31]

This hinders the unfolding procedure as the range of e-by-e $\langle p_T \rangle$ distribution of generated and reconstructed MC data is different from the distribution of raw data measured in the experiment. Figure 4.5 shows this difference in range of MC and raw data distribution. This difference is reflected in the response matrix as it will have the range same as of MC data (as it is like a correlation matrix between generated and reconstructed e-by-e $\langle p_T \rangle$ data), and hence, if and only if the raw distribution falls in its range the unfolding procedure is feasible, which is not in our case.

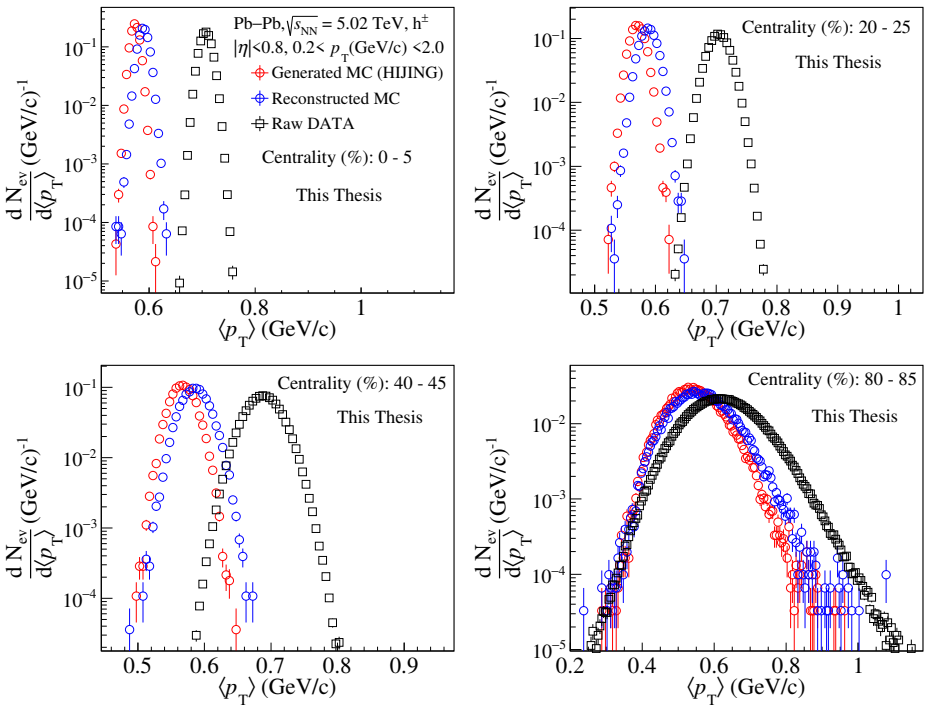

Figure 4.5: Plot shows event-by-event $\langle p_T \rangle$ distribution for three different data-set as mentioned in the legend. The vertical line on marker represent statistical error.

I tried to overcome this problem by applying a simple and naive algorithm as stated below :

1. Make a histogram between e-by-e $\langle p_T \rangle$ and centrality for raw, generated and reconstructed data as shown in fig. (4.6)

2. For each centrality (histogram bin), find the difference between raw and reconstructed e-by-e $\langle p_T \rangle$. Thus the difference is same for all e-by-e $\langle p_T \rangle$ having same centrality.

3. As centrality is a characteristic of an event, check the centrality of event and then add the respective difference to the generated and reconstructed e-by-e $\langle p_T \rangle$ data.

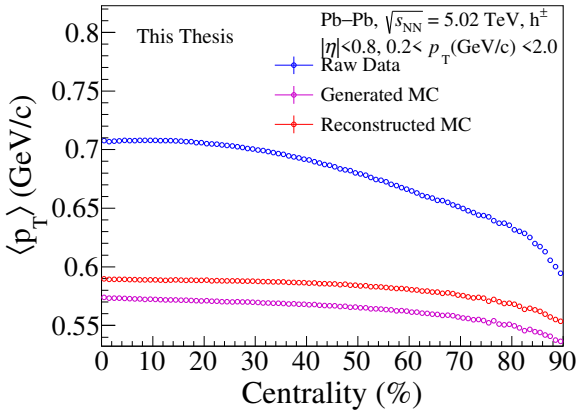

Figure 4.6: Plot shows trend of event-by-event $\langle p_T \rangle$ with centrality for three different data-set as mentioned in the legend.

This way we are just scaling the MC data to the raw data so that the range of response matrix is within the range of raw e-by-e $\langle p_T \rangle$ distribution. After doing these steps , we followed our unfolding procedure with this scaled generated and reconstructed MC data. In the following section of analysis, wherever the MC data is mentioned, it is scaled MC data unless otherwise specified.

4.3.1.2 Closer Test

To ensure the unfolding process works well, we conducted a closer test. The algorithm is the following,

- Divide the MC generated and reconstructed event-by-event $\langle p_t \rangle$ into two halves (Lets say A and B). The selection of event for each half is done randomly to ensure no predetermined preference is present.
- Out of two halves, one data set (A) is used to make response matrix, and the reconstructed values of other half (B) is taken as measured values for unfolding.
- The unfolded distribution (from B) are compared with the generated distribution(from A), and ideally they should be same.

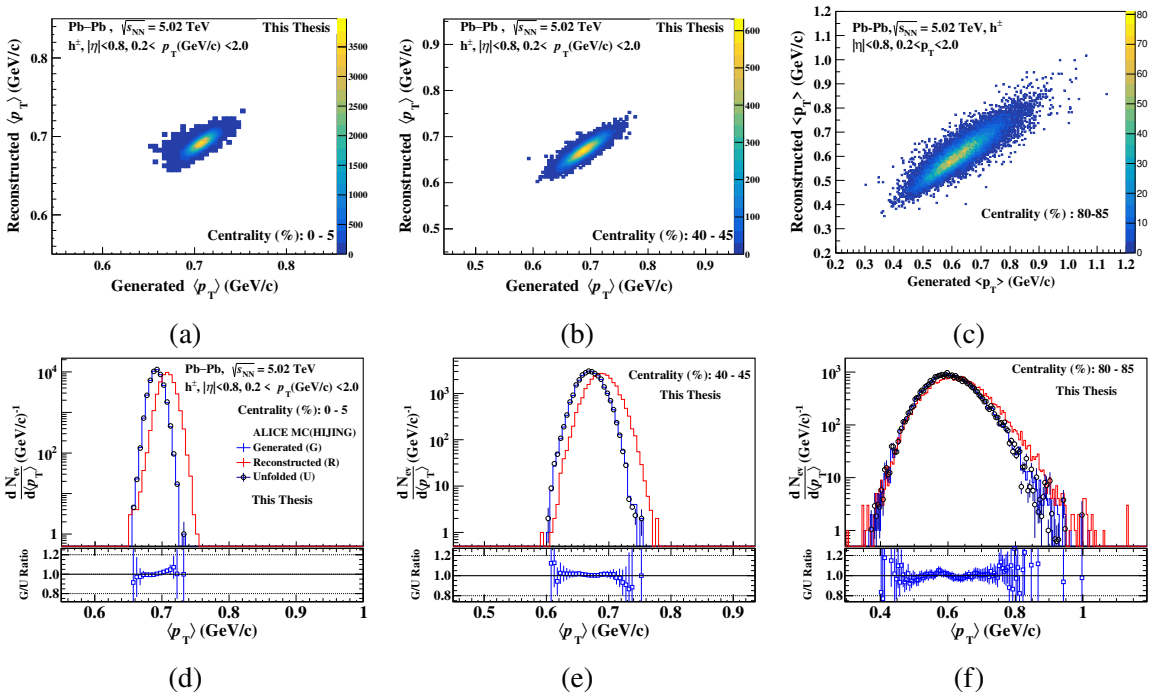

Figure 4.7: The upper plots shows the response matrix for three different centrality bin. In the lower three plots, the upper panel shows the generated, reconstructed and unfolded event-by-event $\langle p_T \rangle$ distribution, using the respective response matrix plotted above them and the lower panel shows their ratio. The vertical line on markers represent statistical error.

Figures 4.7d, 4.7e & 4.7f shows the comparison between the generated and unfolded MC distribution using the mentioned algorithm. The bin-by-bin ratio of generated and unfolded MC distributions are close to 1 (within error bars). Maximum deviation of 20% is seen for data points far away from the distribution mean.

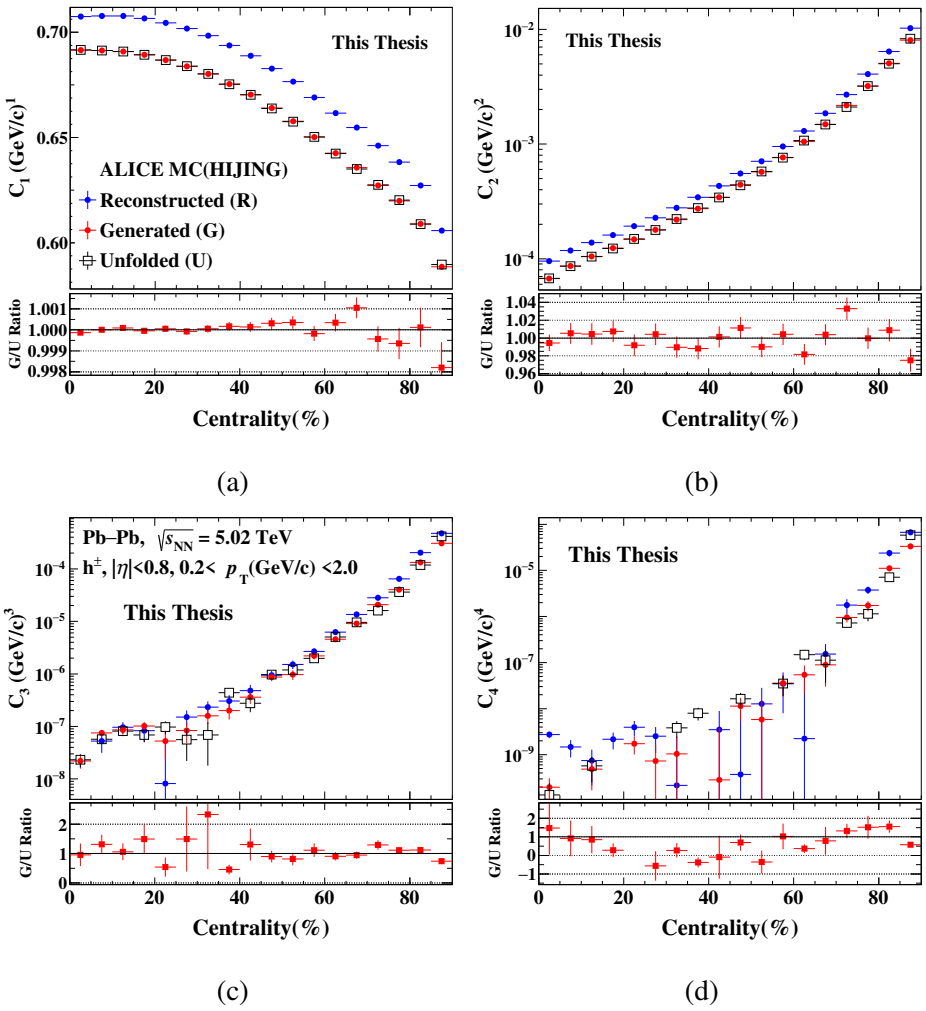

Figure 4.8: The upper panel of the plots show first four cumulants of MC generated, reconstructed and unfolded event-by-event $\langle p_T \rangle$ distribution for respective centrality bin and the lower panel shows their ratio. The Y-axis of higher order cumulants are in log scale. The vertical line on markers represent statistical error.Missing markers in higher order cumulants indicates the values are negative.

As stated previously in the algorithm of closer test, a perfect unfolding leads the unfolded e-by-e $\langle p_T \rangle$ distributions of MC to be same as the generated MC distribution. This directly implies that the cumulants of both the distribution to be same as well. Therefore a better comparison is made by reviewing their first four cumulants as shown in figure (4.8). C_1 and C_2 are same, within 0.2 % and 4 % deviation as seen in the generated by unfolded cumulants ratio plots in sub-fig. 4.8a and 4.8b respectively. C_3 is fairly comparable within

error range but the ratio plot in sub-fig. 4.8c shows strong deviation in 15-20 % centrality range. C_4 values are negative for few centrality bins below 30%. Further the ratio plot in sub-fig. 4.8d reveals the strong deviation between them. The strong deviation of C_3 and C_4 is evident from low MC statistics used in unfolding.

4.3.1.3 ALICE data Unfolding

The response matrix for unfolding raw (measured in experiment) data looks the same as provided in fig. (4.7) just that it is made with full MC statistics. The unfolded distribution for three different centrality is shown in fig. (4.9).

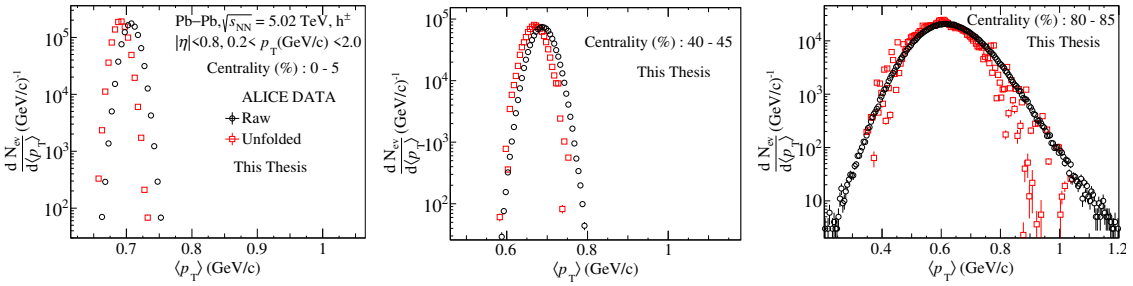

(a) (b) (c)

Figure 4.9: Plots show the raw and unfolded event-by-event $\langle p_T \rangle$ distribution. The vertical line on markers represent statistical error

Figure 4.10 shows the first four cumulants of raw and unfolded e-by-e $\langle p_T \rangle$ distributions. The trend in C_1 and C_2 is same for both the distribution. Their ratio have a constant value for each centrality bin. In case of C_3, the trend in the unfolded and raw is same, but there is clearly large deviation for centrality below 45% as seen in the ratio plot. Meanwhile C_4 shows strong deviation. Fairly in most centrality bins, the unfolded C_4 are negative, and a negative constant ratio shows that the trend is opposite than that of raw i.e, it is decreasing with centrality. The subplot in the upper panel of fig. (4.10d) has the y-axis in linear scale. This shows the negative values of C_4 which is missing in the plot. Clearly, the study of higher cumulants are very skeptical for the unfolded distributions.

The reason for this result is due to very low MC statistics. The HIJING MC data set available in ALICE is about 3 million of which ~ 1.4 million are good events to be used for our analysis. Unfolding is good when MC statistics and raw statistics are large and

comparable. Therefore to unfold a large raw data (17 million in this analysis), the available MC statistic which have the detector effects are very low.

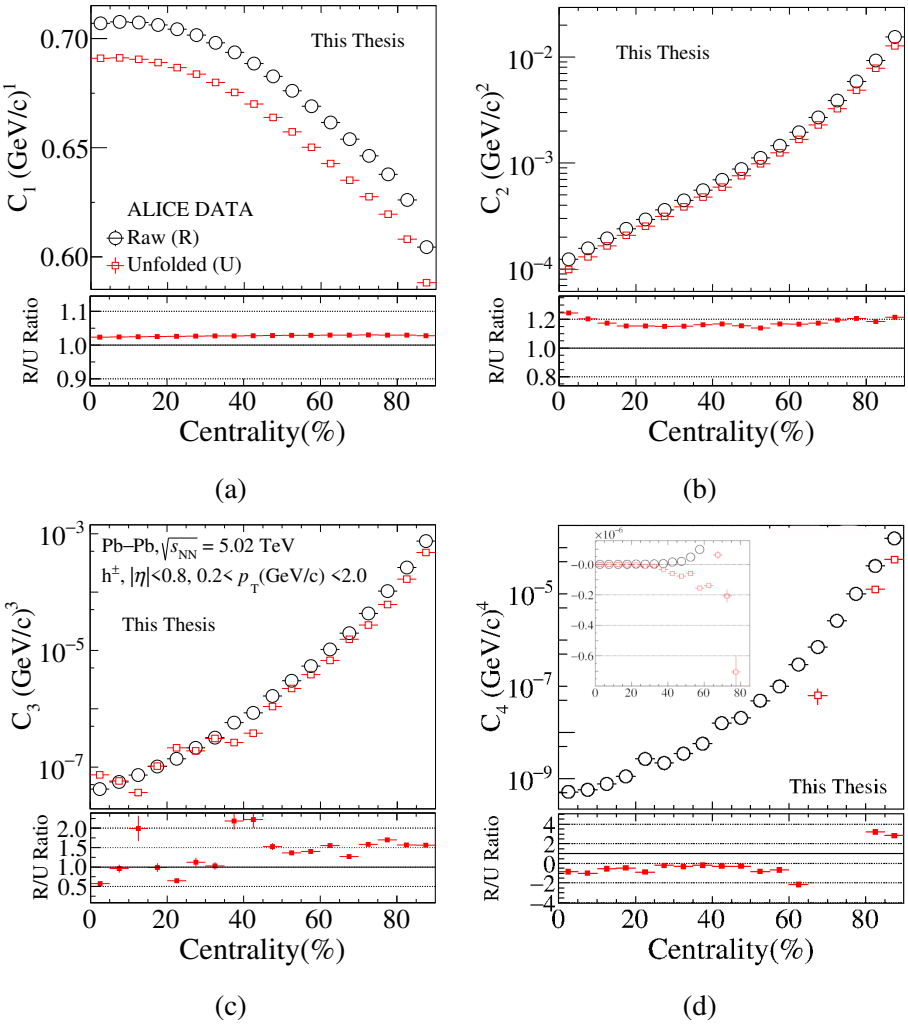

Figure 4.10: The upper panel in the plots show the cumulants of raw and efficiency corrected (by unfolding) event-by-event $\langle p_{\mathrm{T}} \rangle$ distributions and the lower panel shows their ratio. The y-axis of higher order cumulants are in log scale. The vertical line on markers represent statistical error. The sub-plot in the upper panel of the plot (d) has y-axis in linear scale; it shows the negative values which are missing in the plot.

4.3.2 Ratio Method

A more simplistic approach than unfolding is used to remove the detector effects. In this approach we assume relation (4.1) holds for all cumulants.

$$\frac{C_i^{rec}}{C_i^{gen}} = \frac{C_i^{raw}}{C_i^{cor}} \qquad i \in \{1, 2, 3, 4\} \tag{4.1}$$

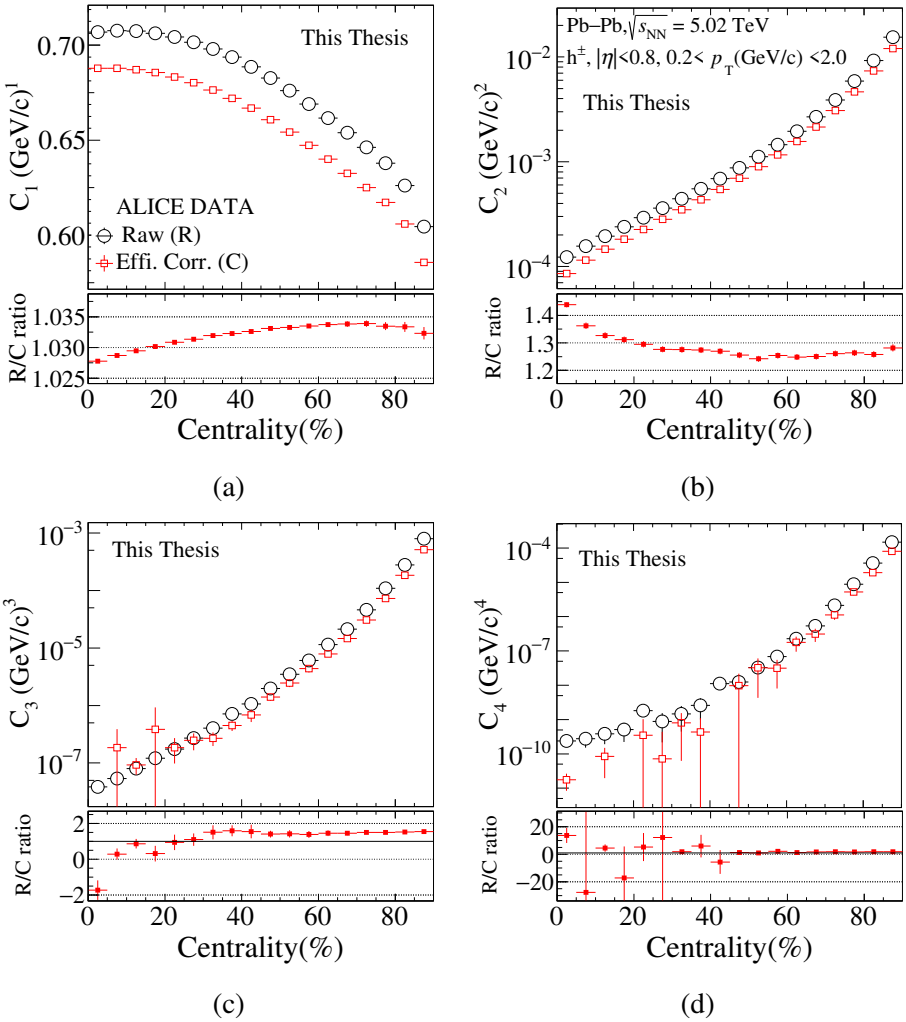

Figure 4.11: The upper panel in the plots show the cumulants of raw and efficiency corrected (by ratio method) event-by-event $\langle p_T \rangle$ distributions and the lower panel shows their ratio. The y-axis of higher order cumulants are in log scale. The vertical line on markers represent statistical error. Missing markers in higher order cumulants indicates the values are negative.

Hence, the corrected cumulant (C^{cor}) is easily calculated by the following equation,

$$C_i^{cor} = \frac{C_i^{raw}}{C_i^{rec}/C_i^{gen}} \qquad i \in \{1, 2, 3, 4\} \tag{4.2}$$

Here, C^{gen}, C^{rec} and C^{raw} are the cumulants of generated MC, reconstructed MC and raw e-by-e $\langle p_T \rangle$ distribution. The cumulants of these three distribution are centrality bin width corrected (CBWC). Therefore, the corresponding corrected cumulants which we obtain are also CBWC. The details about this correction is provided in paper [32].

The corrected C_1 and C_2 follows the same trend as of the raw cumulants. For C_3, the corrected does follow the trend of raw cumulants but have large deviation at low centrality bins (< 20%). In this method also we find that C_4 is negative for few centrality bins, despite this the corrected follows the trend of raw at higher centrality bins (>50 %).

Chapter 5

Mean transverse momentum fluctuations

It was observed that the event-by-event (e-by-e) mean transverse momentum ($\langle p_{\mathrm{T}} \rangle$) distribution for Pb-Pb collision measured by NA49 experiment, SPS, CERN was explained by Gamma Distribution (GD) function ($f_{\Gamma}(x, \lambda, \alpha)$) and mixed event distribution (a distribution solely acting as a statistical baseline) very well. Another interesting point noted by M. J. Tannenbaum [2] was that the inclusive single particle p_{T} distribution is given as $\frac{d\mathrm{N}_{ch}}{p_{\mathrm{T}}} = \lambda^2 e^{-\lambda p_{\mathrm{T}}}$. This is clearly a GD with $\lambda = 2$. These two points motivated author to look into the properties of the GD. As a result the special properties of GD concluded that if the emitted particles are statistically independent and p_{T} follow gamma distribution then e-by-e $\langle p_{\mathrm{T}} \rangle$ should follows GD or stated differently GD acts as a statistical baseline for e-by-e $\langle p_{\mathrm{T}} \rangle$ [2].

Gamma distribution with variable x ($0 \leq x \leq \infty$) and parameters λ (> 0) & α (> 0) is defined as,

$$f_{\Gamma}(x, \lambda, \alpha) = \frac{\lambda}{\Gamma(\alpha)} (\lambda x)^{\alpha - 1} e^{-\lambda x} \tag{5.1}$$

The cumulants for the Gamma distribution is calculated by the following relations (5.2 (for derivation see D.3a).

$$\mathrm{C}_1 = \frac{\alpha}{\lambda} \tag{5.2a}$$

$$\mathrm{C}_2 = \frac{\alpha}{\lambda^2} \tag{5.2b}$$

$$\mathrm{C}_3 = \frac{2\alpha}{\lambda^3} \tag{5.2c}$$

$$\mathrm{C}_4 = \frac{6\alpha}{\lambda^4} \tag{5.2d}$$

5.1 In pp system

Similar analysis of event-by-event $\langle p_T \rangle$ in proton-proton collisions has been implemented for the event generator models in the subsequent plots. Every plot (fig.5.1-5.4) consists of event-by-event $\langle p_T \rangle$ distribution for six different multiplicity percentile classes. Each distribution has been fitted with Gamma distribution. The fitted parameter along with χ^2/ndf value has been provided in the upper right corner of each subplot. Best fit is considered when the χ^2/ndf is close to zero. The theoretical details about χ^2/ndf test to find best fit is given in appendix F.

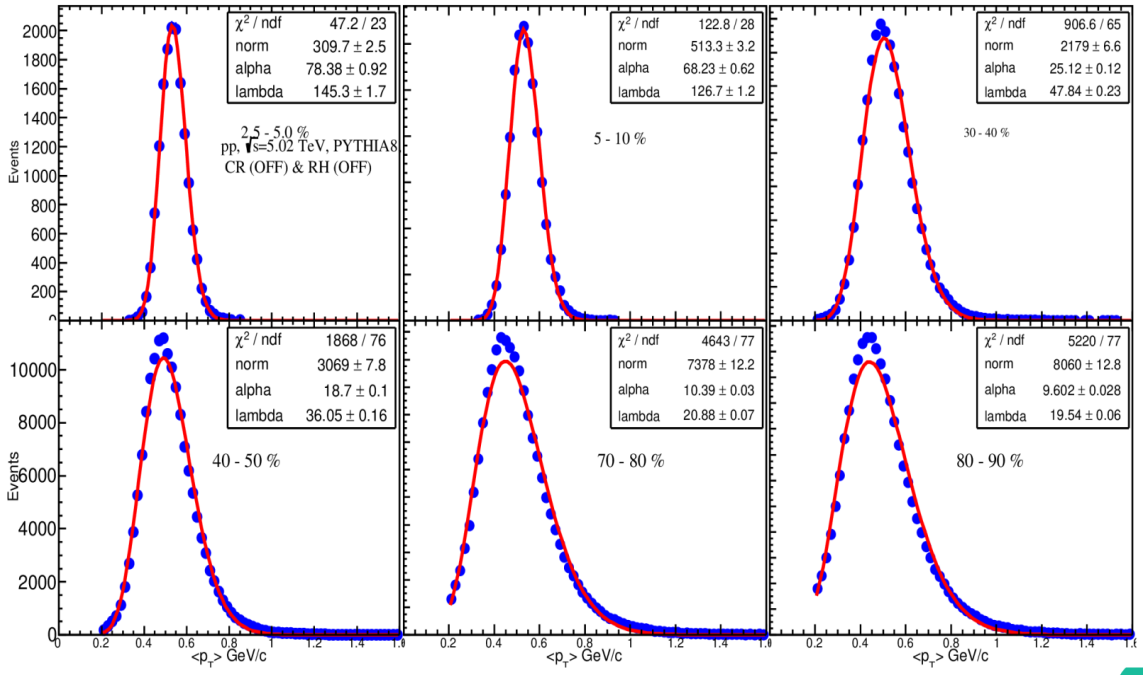

Figure 5.1: Event-by-event $\langle p_T \rangle$ distribution for events generated with configuration CR-OFF and RH-OFF and its corresponding fit function. The y-axis represent number of events and x-axis represent event-by-event $\langle p_T \rangle$.

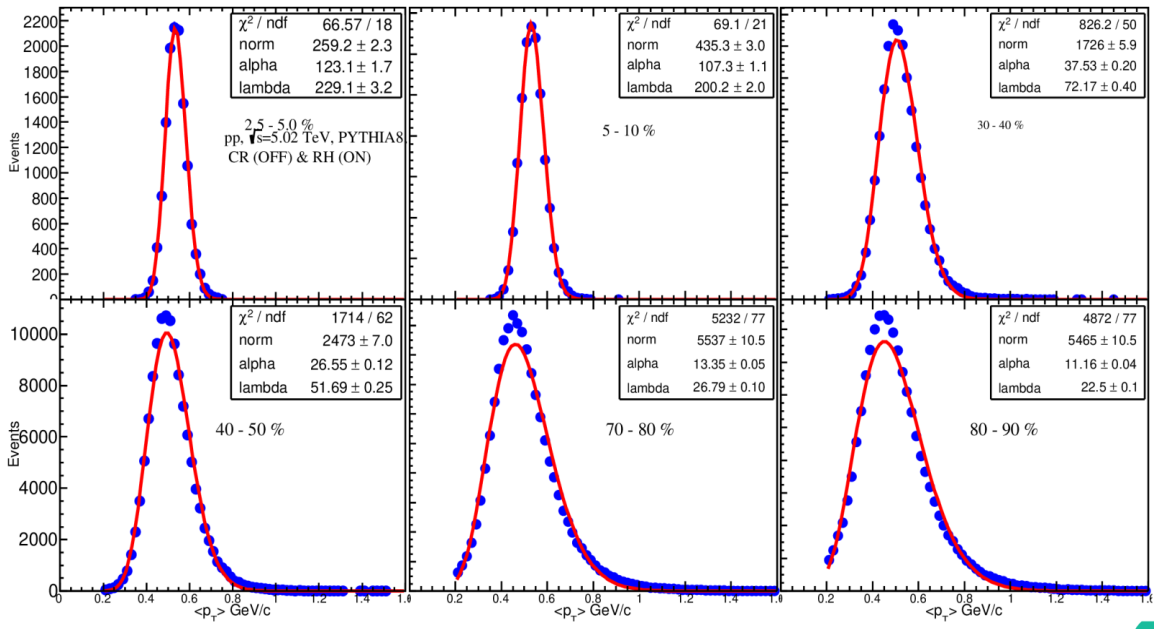

Figure 5.2: Event-by-event $\langle p_T \rangle$ distribution for events generated with configuration CR-OFF and RH-ON and its corresponding fit function. The y-axis represent number of events and x-axis represent event-by-event $\langle p_T \rangle$.

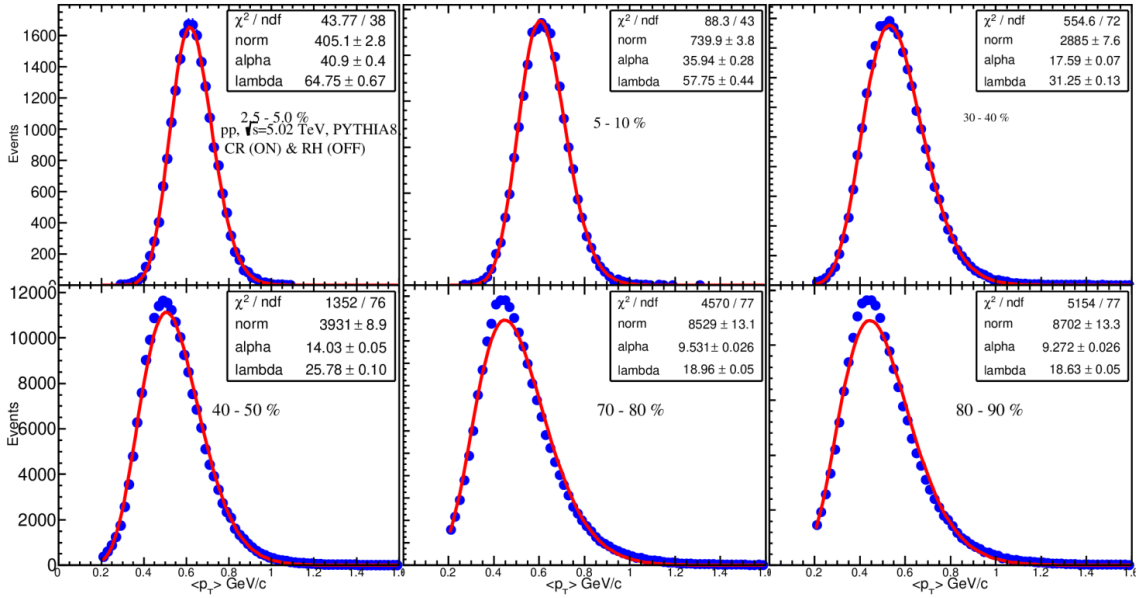

Figure 5.3: Event-by-event $\langle p_T \rangle$ distribution for events generated with configuration CR-ON and RH-OFF and its corresponding fit function. The y-axis represent number of events and x-axis represent event-by-event $\langle p_T \rangle$.

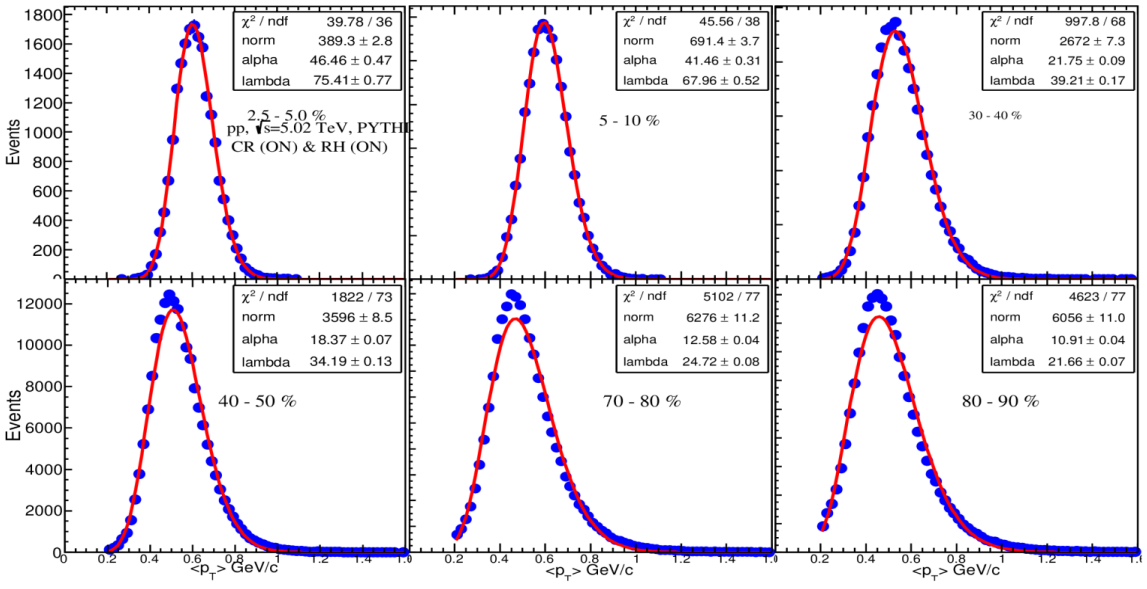

Figure 5.4: Event-by-event $\langle p_T \rangle$ distribution for events generated with configuration CR-ON and RH-ON and its corresponding fit function. The y-axis represent number of events and x-axis represent event-by-event $\langle p_T \rangle$.

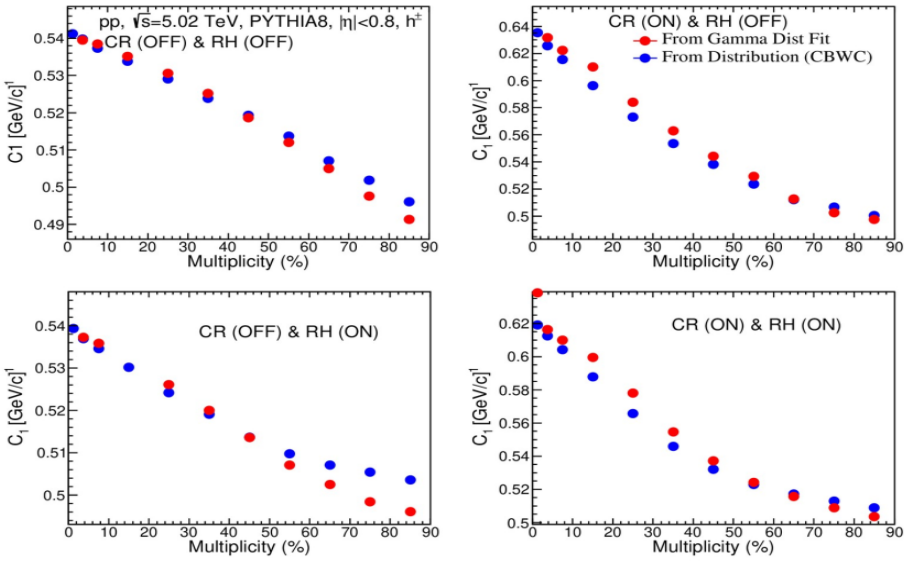

Figure 5.5: C_4 variation with multiplicity percentile for all four model configuration used for particle production in PYTHIA8. The x-axis represent multiplicity percentile.

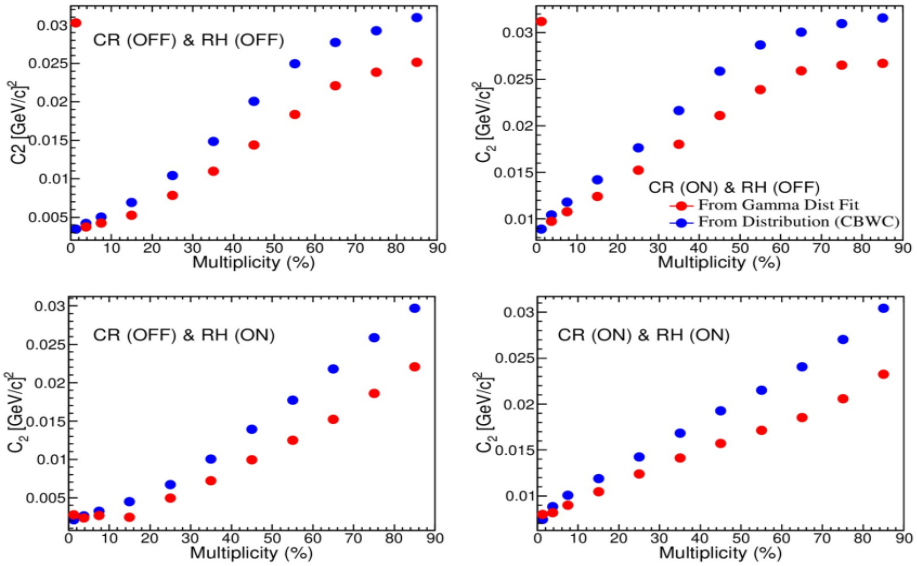

Figure 5.6: C_2 variation with multiplicity percentile for all four model configuration used for particle production in PYTHIA8. The x-axis represent multiplicity percentile.

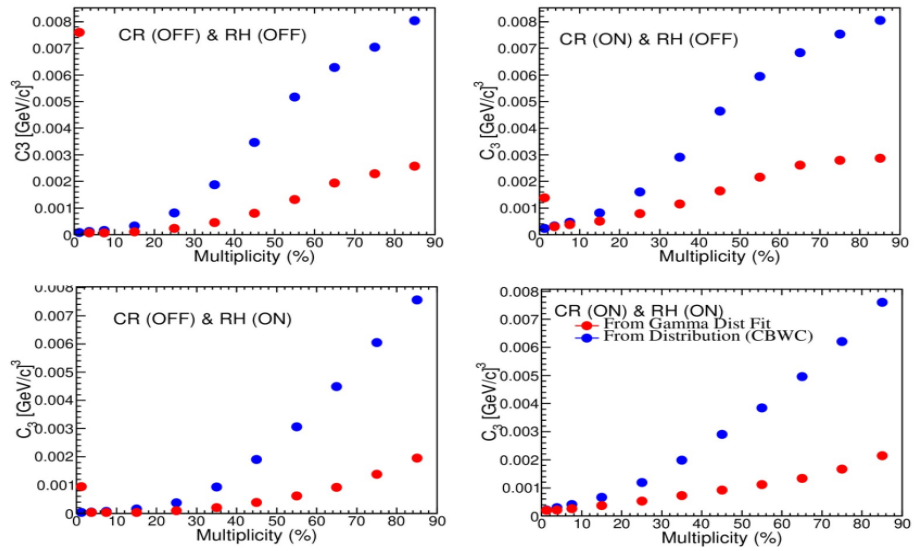

Figure 5.7: C_3 variation with multiplicity percentile for all four model configuration used for particle production in PYTHIA8. The x-axis represent multiplicity percentile.

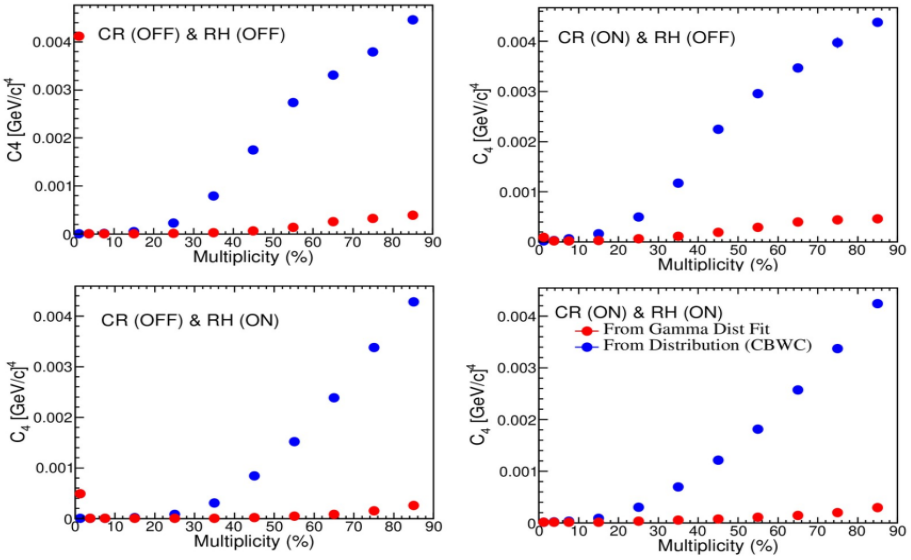

Figure 5.8: C_4 variation with multiplicity percentile for all four model configuration used for particle production in PYTHIA8. The x-axis represent multiplicity percentile.

The unusually large difference in the lower multiplicity class is due to bad fitting and/or low statistics. It is observed that the mean (C_1) of e-by-e $\langle p_T \rangle$ distribution and the Gamma fitted function are nearly comparable. But for the higher cumulants, C_2, C_3 and C_4 the difference grows with centrality. Therefore, it can be inferred that the particle emitted in each event are not independently emitted.

5.2 In Pb–Pb system

From the first two cumulants C_1 and C_2 of e-by-e $\langle p_T \rangle$, the parameters λ and α are calculated. If the e-by-e $\langle p_T \rangle$ distribution follows GD then higher order cumulants calculated from these parameters should match the cumulants calculated from the distribution itself. It was seen earlier that C_3 and C_4 of corrected e-by-e $\langle p_T \rangle$ distribution from both the method, unfolding and ratio, bears lot skepticism due to low MC statistics. Still this analysis is also done to understand what C_3 and C_4 values will look when corrected e-by-e $\langle p_T \rangle$ follows GD, statistical baseline.

Out of all the cumulants calculated from the parameters, C_1 and C_2 will match with the C_1 and C_2 calculated from the e-by-e $\langle p_T \rangle$ distribution for obvious reasons. This is clearly

seen in figures 5.9 and 5.10.

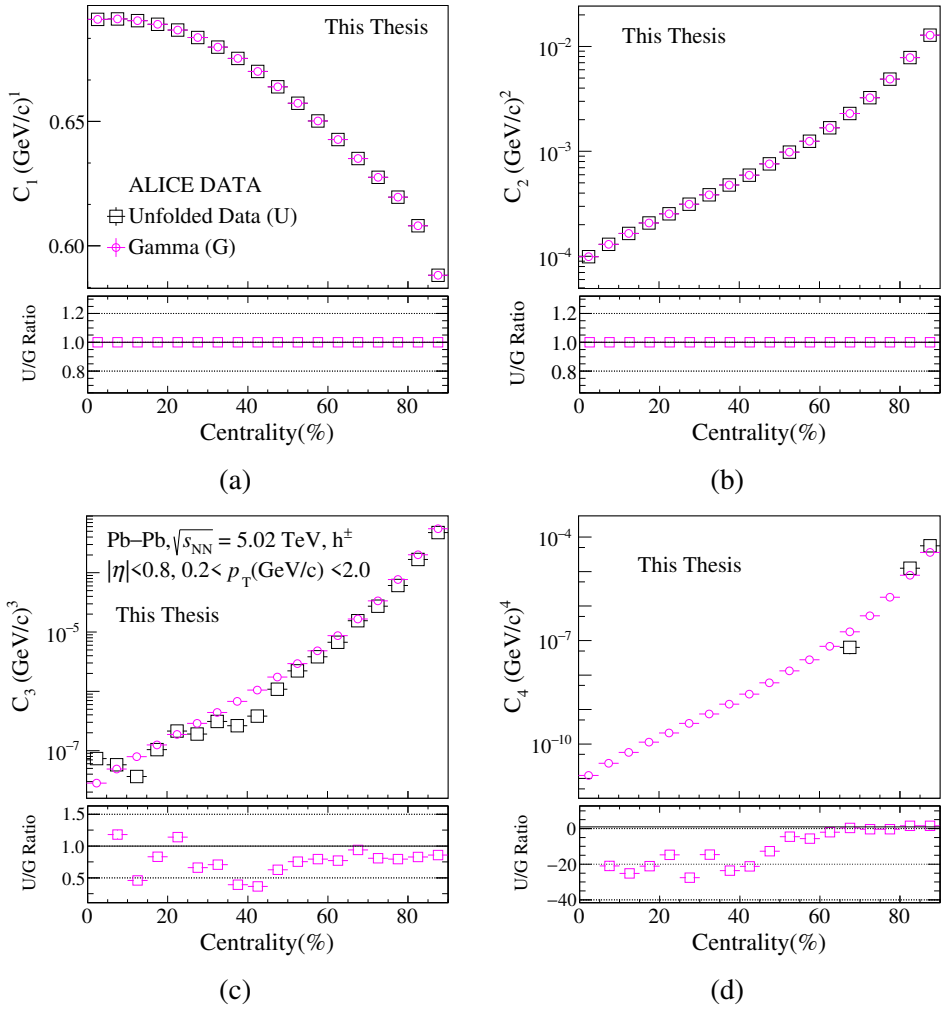

Figure 5.9: The upper panel in the plots show the variation of corrected (by ratio method) cumulants with statistical baseline and lower panel shows their ratio. The y-axis of higher order cumulants is in log scale. Upper two plots are the "closer test" for the comparison procedure. The black markers missing in plot (d) is due to the values are negative.

Only C_3 can be compared fairly as most of the C_4 values of corrected distribution from the method are negative. The trend and order of the values are same but for many centrality classes, the values deviate each other by more than 20 % as shown in ratio plot of fig. (5.9c). The values of C_4 are negative so in log scale they are not visible as shown in fig. (5.9d), and from the ratio plot it can only inferred that the order of C_4 are same.

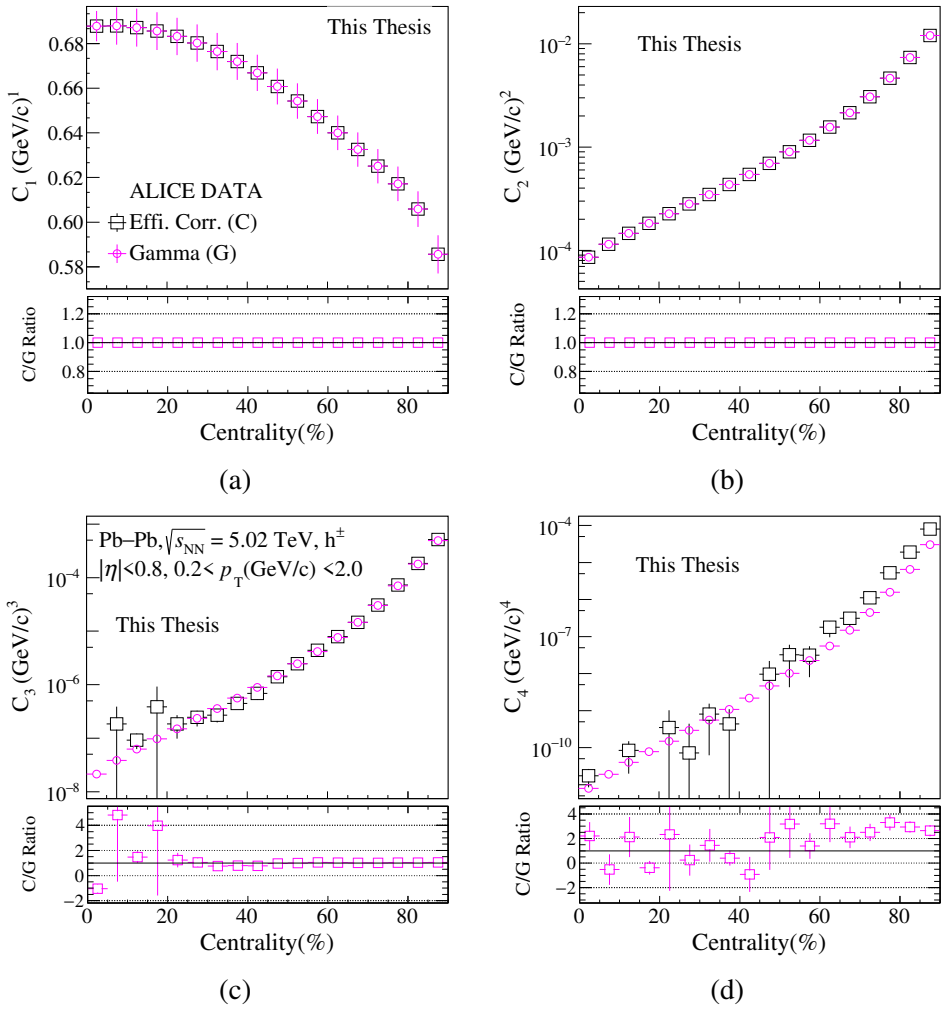

Figure 5.10: The upper panel in the plots show the variation of corrected (by ratio method) cumulants with statistical baseline and lower panel shows their ratio. The y-axis of higher order cumulants is in log scale. Upper two plots are the "closer test" for the comparison procedure. Missing markers in higher order cumulants indicates the values are negative.

In case of corrected data from ratio method, C_3 values from the distribution is comparable to the C_3 calculated from GD parameters but not for centrality classes less than 20% as there is large deviation of C_3 values (calculated from distribution) from the general trend 5.10c. A better comparison can be made for C_4 values as there exits a general trend in C_4 with centrality 5.10d. The C_4 are in same order and are slightly comparable within error bars.

Chapter 6

Summary

In this thesis,proton-proton collision events were simulated using PYTHIA8 event generator. At first we briefly looked into color reconnection (CR) and rope hadronization (RH) model for particle production present in PYTHIA8. Then, effect of these two models was observed by taking four different configuration during event generation:

- CR-ON and RH-OFF (default configuration in PYTHIA8)
- CR-ON and RH-ON
- CR-OFF and RH-ON
- CR-OFF and RH-ON

Effect of each model was prominently observed in higher multiplicity events (low multiplicity percentile class), and RH increases particle production in both CR(On and CR(OFF) configuration. The cumulants of event-by-event (e-by-e) mean transverse momentum ($\langle p_{\mathrm{T}} \rangle$) shows a common trend with multiplicity percentile in each configuration. C_1 decreases with multiplicity percentile, and C_2, C_3 and C_4 increases with multiplicity percentile. However, RH decreases the value of each cumulant. Also in low multiplicity percentile classes, C_1 and C_2 are higher when CR model is used for particle production.

Statistical fluctuation are inherent in each observation due to various unavoidable reasons [14, 1]. To check whether the observed fluctuations are only statistical, e-by-e $\langle p_{\mathrm{T}} \rangle$ distribution is compared with gamma distribution (GD), a baseline for statistical fluctuation.

In pp collisions, the e-by-e $\langle p_{\mathrm{T}} \rangle$ distribution is fitted with gamma distribution function, and then the cumulants of e-by-e $\langle p_{\mathrm{T}} \rangle$ distribution and fit curve are compared. Independent of the model configuration used for particle production in PYTHIA8, there exits a large difference in C_3 and C_4 of e-by-e $\langle p_{\mathrm{T}} \rangle$ distribution and gamma fit curve, and the difference grows with multiplicity percentile.

In case of Pb-Pb collisions a different method is applied, first the parameters of GD are calculated from efficiency corrected C_1 and C_2 , then C_3 and C_4 constructed from these parameters are compared with the ones calculated from e-by-e $\langle p_T \rangle$ distribution. When the data is corrected by unfolding method, C_3 is fairly comparable but with deviation upto 50% in collisions with centrality < 50%, and the unreasonable values of corrected C_4 don't lead to any comparison. In ratio method, the corrected C_3 (within error bars) are in good comparison with C_3 calculated from gamma parameters but have large deviation in central collisions (centrality < 20%), while C_4 is slightly comparable within error bars.

The trend of cumulants with multiplicity percentile in pp collision is same as the trend of cumulants with centrality in Pb–Pb collisions. In central and semi-peripheral collision, higher order cumulants, C_3 and C_4 in Pb–Pb collision are much lower than cumulants (for any modal configuration) in pp collision. Also the comparison with statistical baseline shows that in pp collisions, the deviation of higher order cumulants from statistical baseline increases with multiplicity percentile. This dependence with centrality is absent in Pb–Pb collisions. So far two naive conclusions can be said, first high multiplicity proton-proton collisions show similar characteristics as peripheral heavy-ion collisions and as system size increases from pp to Pb–Pb, e-by-e fluctuations is dominated by statistical part.

Appendix A

Lorentz transformations calculations

All variables defined in the later section are in natural units i.e., $c = \hbar = 1$

If we choose the beam direction to be z-axis and the particle is moving with speed β then Lorentz transformation laws state that,

$$p'_z = \gamma(p_z - \beta p_0) \tag{A.1}$$

$$p'_x = p_x \tag{A.2}$$

$$p'_y = p_y \tag{A.3}$$

$$p'_0 = \gamma(p_0 - \beta p_z) \tag{A.4}$$

Now suppose we observe that under Lorentz transformation from lab frame (F) to a frame (F') which is boosted in the z-direction with velocity β, the rapidity in F' is given as

$$\begin{aligned} y' &= \frac{1}{2}\ln\left(\frac{p'_0 + p'_z}{p'_0 - p'_z}\right) \\ &= \frac{1}{2}\ln\left(\frac{\gamma(p_0 - \beta p_z) + \gamma(p_z - \beta p_0)}{\gamma(p_0 - \beta p_z) - \gamma(p_z - \beta p_0)}\right) \\ &= \frac{1}{2}\ln\left(\frac{p_0(1-\beta) + p_z(1-\beta)}{p_0(1+\beta) - p_z(1+\beta)}\right) \\ &= \frac{1}{2}\ln\left[\frac{1-\beta}{1+\beta} + \frac{p_0 + p_z}{p_0 - p_z}\right] \\ &= y - \frac{1}{2}\ln\frac{1+\beta}{1-\beta} \end{aligned}$$

Therefore,

$$\boxed{y' = y - y_\beta \quad \text{here,} y_\beta = \frac{1}{2}\ln\frac{1+\beta}{1-\beta}} \tag{A.5}$$

y_β is often referred to as " rapidity of the moving frame". This relation is same as that of Galilean transformation of velocities ($\beta \ll 1$). therefore, rapidity is often said as relativistic measure of the " velocity " of the particle [33].

Appendix B

Bayes Unfolding Theory

Lets assume the following notations, $P(C_i)$ as probability of cause C_i and $P(E|C_i)$ as the conditional probability of cause C_i to produce the effect E. If we observe the effect E, then the probability that is due to cause C_i is given by Bayes' theorem as

$$P(C_i|E) = \frac{P(E|C_i) \cdot P(C_i)}{\sum_l^{n_c} P(E|C_l) \cdot P(C_l)} \tag{B.1}$$

On observing n(E) no. of events with effect E, the expected no. of events for each cause is

$$\hat{n}(C_i) = n(E) \cdot P(C_i|E) \tag{B.2}$$

If the measurement has n_E possible number of effects $E_j (j = \{1, 2, \ldots n_E\})$ for the cause C_i. Bayes' formula holds for each of the effect and thus $P(C_i|\, E_j)$ can be calculated by eq. (B.1). Again with the initial probability of causes taken as $P_0(C_i)$, eq. (B.1) is written as

$$P(C_i|E_j) = \frac{P(E_j|C_i) \cdot P_0(C_i)}{\sum_l^{n_c} P(E|C_l) \cdot P_0(C_l)} \tag{B.3}$$

The probabilities $P(C_i|E_j)$ referred as **Smearing Matrix** , **S** elements (S_{ij}) and $P(E_j|E_i)$ referred as **Response Matrix** , **S** elements (E_{ji}). Suppose after N_{obs} experimental observations, the frequency of n_E effects are $n(E_1), n(E_2), \ldots, n(E_{E_n})$. Using eq. (B.2), the expected frequency for each cause C_i is given as,

$$\hat{n}(C_i) = \frac{1}{\epsilon_i} \sum_{j=1}^{n_E} n(E_j) \cdot P(C_i|E_j) \qquad \epsilon_i \neq 0 \tag{B.4}$$

Here $\epsilon_i \equiv \sum_{j=1}^{n_E} P(E_j|C_i)$ is the efficiency of detecting a cause for all possible effects. $\epsilon_i \in [0, 1]$ and if it is equal to 0 then $\hat{n}(C_i)$ is 0, as none of the effect is caused due to C_i. These $\hat{n}(C_i)$ are the **unfolded frequencies**. Now the true total number of observations is $\hat{N}_{true} = \sum_{i=1}^{n_C} \hat{n}(C_i)$ and therefore the estimated final probabilities of the causes are

$$\hat{P}(C_i) = \frac{\hat{n}(C_i)}{\hat{N}_{true}} \tag{B.5}$$

This final distribution $P_0(C)$ depends how the initial distribution $P_0(C)$ is chosen. Therefore, the unfolding gives better results if the initial distribution is closer to the "true" distribution. However guessing the initial distribution is always not possible therefore an iterative method is applied [34]:

1. A initial distribution $P_0(C)$ is chosen. Then the initial expected no. of events for causes is $n_0(C_i) = P_0(C_i) \cdot N_{obs}$.
2. $\hat{n}(C_i)$ and $\hat{P}_0(C_i)$ are calculated using eq. (B.4) and (B.5) respectively.
3. A χ^2 comparison is made between $\hat{n}(C_i)$ and $\hat{n}_0(C_i)$.
4. Check the χ^2 is "small enough". If not replace $\hat{P}_0(C_i)$ with $\hat{P}(C_i)$ and $\hat{n}_0(C_i)$ with $\hat{n}(C_i)$, and start the step 2 again untill desired χ^2 is obtained.

Appendix C

Unfolding Related Plots

C.1 Response Matrices

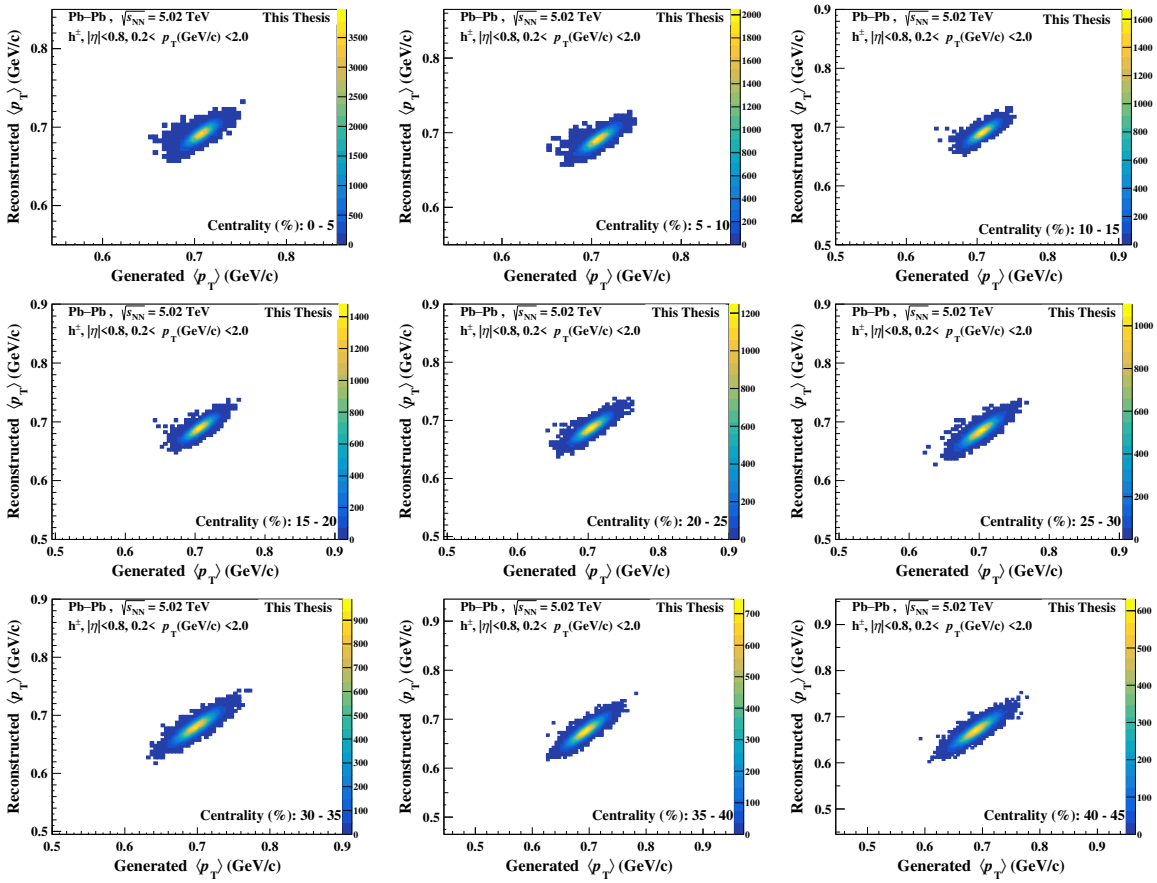

Figure C.1: Plots shows the response matrix made with generated and reconstructed event-by-event $\langle p_T \rangle$ MC data.

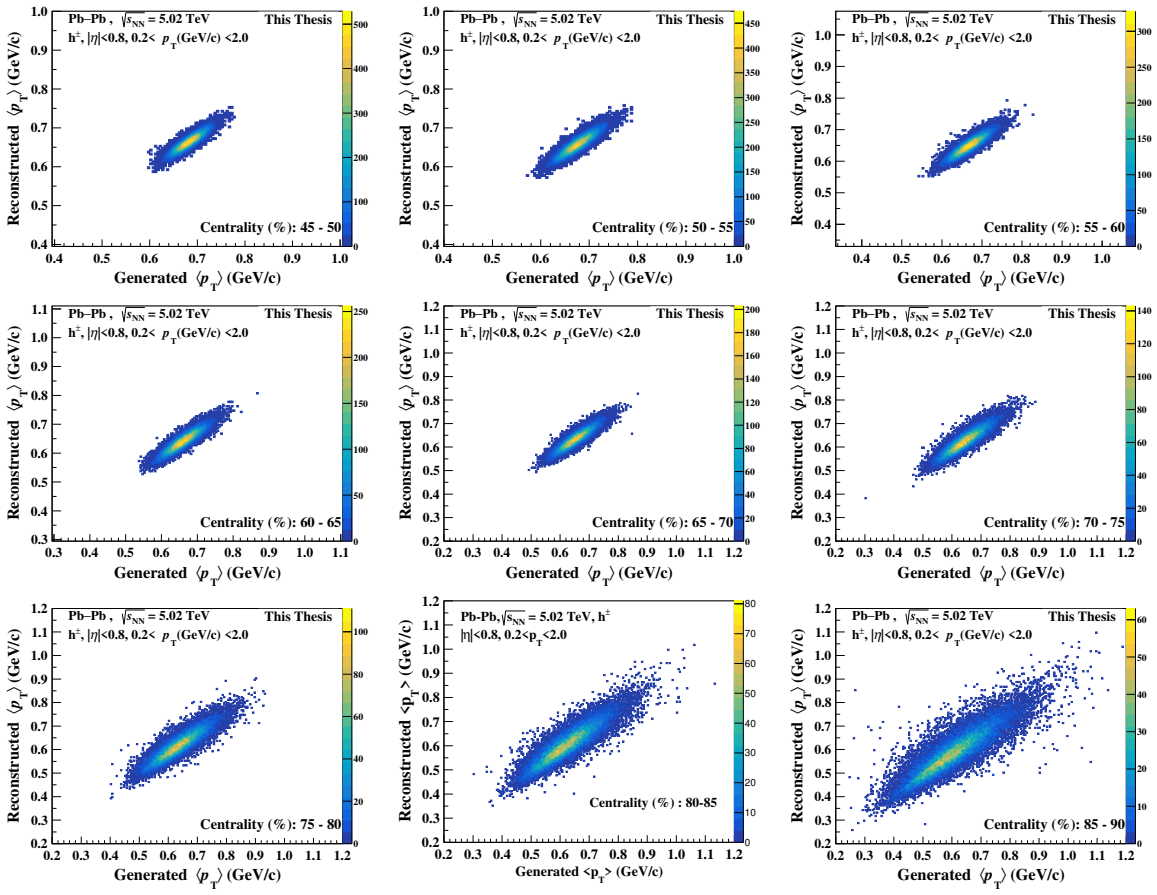

Figure C.2: Plots shows the response matrix made with generated and reconstructed event-by-event $\langle p_T \rangle$ MC data.

C.2 Unfolded MC Plots

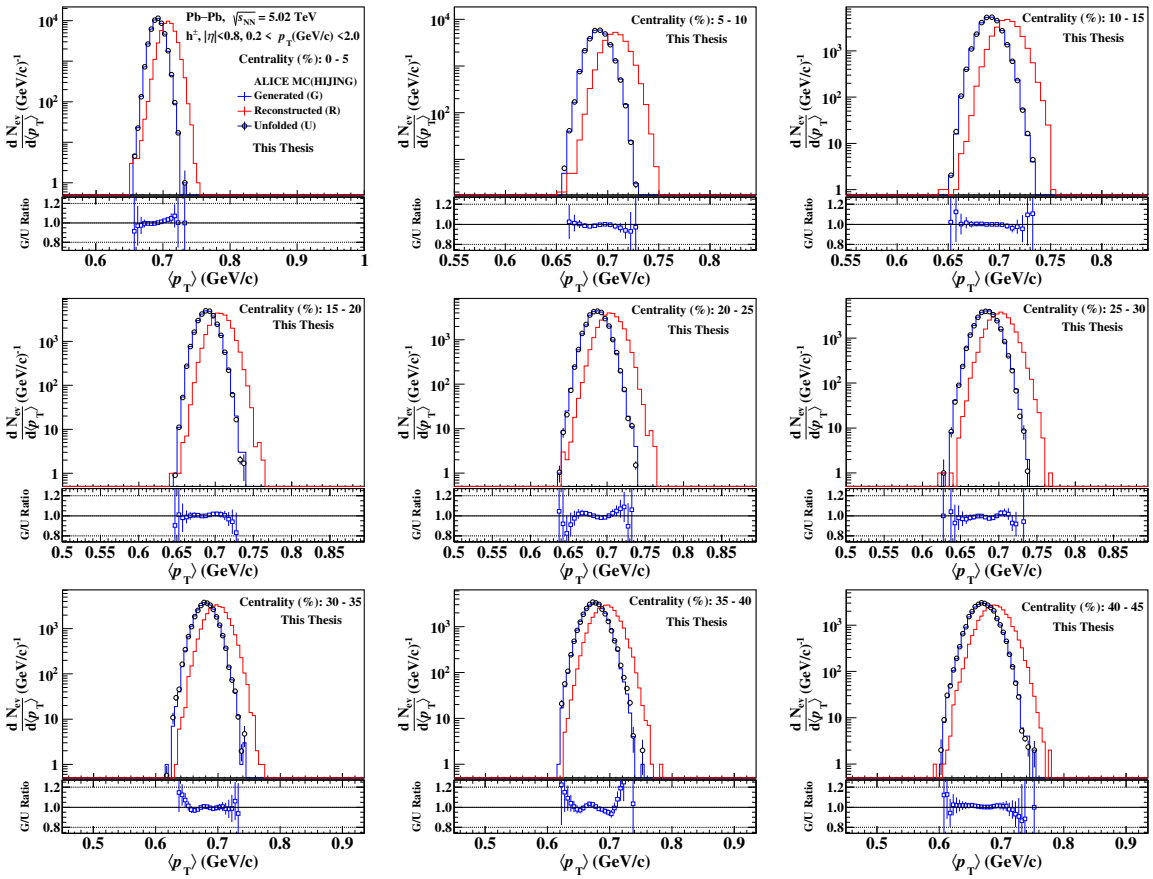

Figure C.3: In the plots, the upper panel shows the generated, reconstructed and unfolded event-by-event $\langle p_T \rangle$ distribution and the lower panel shows their ratio. The vertical line on markers represent statistical error.

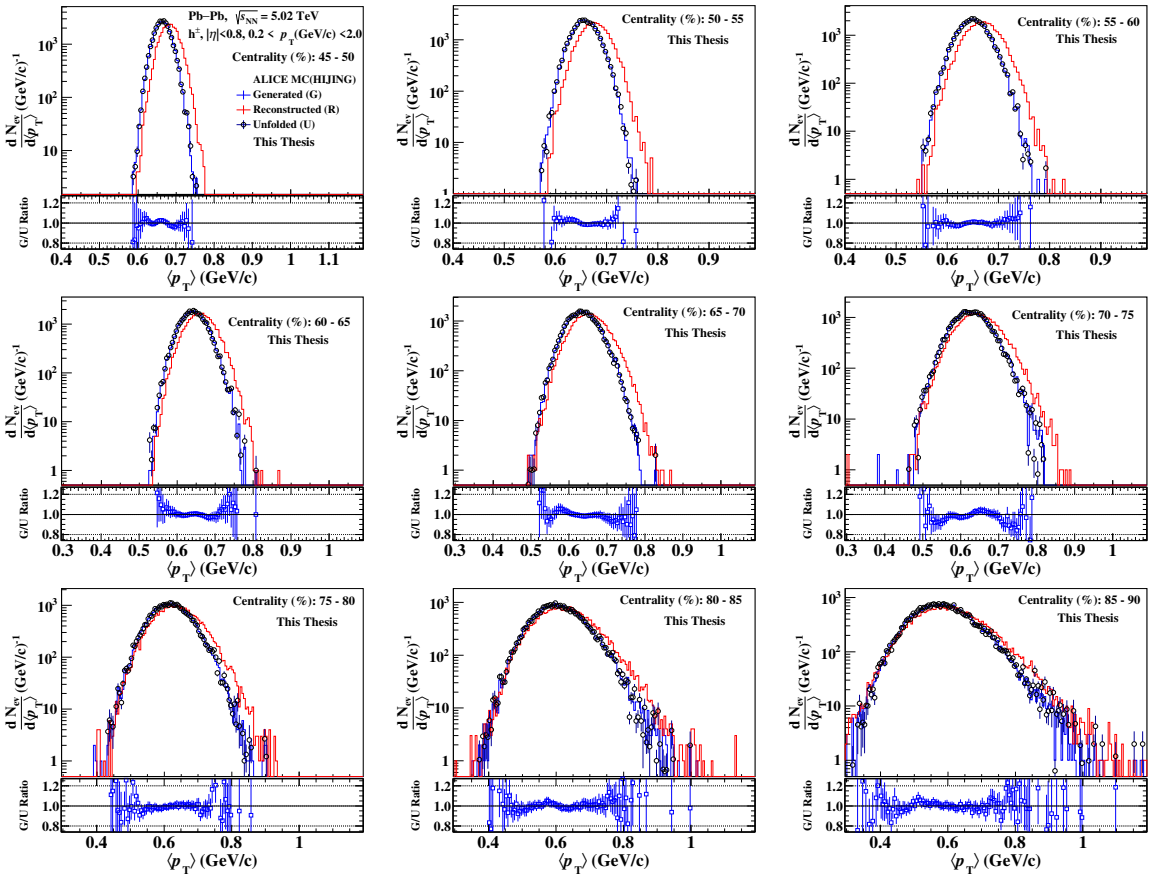

Figure C.4: In the plots, the upper panel shows the generated, reconstructed and unfolded event-by-event $\langle p_T \rangle$ distribution and the lower panel shows their ratio. The vertical line on markers represent statistical error.

Appendix D

Gamma Distribution Cumulants

Using the definition **??**, the characteristic function of Gamma distribution is given as,

$$\begin{aligned}
P_{\alpha,\lambda}(k) &= E\left[e^{-\iota kx}\right] \\
&= \int_0^\infty e^{-\iota kx}\left(\frac{\lambda^\alpha x^{\alpha-1}e^{-\lambda x}}{\Gamma(\alpha)}\right) \\
&= \frac{\lambda^\alpha}{\Gamma(\alpha)}\int_0^\infty e^{-\iota kx}e^{-\lambda x}x^{\alpha-1} \\
&= \frac{\lambda^\alpha}{\Gamma(\alpha)}\int_0^\infty e^{-t}\frac{t^{\alpha-1}}{(\lambda+\iota k)^{\alpha-1}}\frac{dt}{(\alpha+\iota k)} \quad t = (\lambda+\iota k) \\
&= \frac{\lambda^\alpha}{\Gamma(\alpha)(\lambda+\iota k)^\alpha}\int_0^\infty e^{-t}t^{\alpha-1}dt \quad \text{here the integral part is definition of } \Gamma(\alpha)
\end{aligned}$$

Therefore,

$$P_{\alpha,\lambda}(k) = \left(\frac{\lambda}{\lambda+\iota k}\right)^\alpha \tag{D.1}$$

The cumulant generating function is defined as,

$$\Phi(k) = \ln\left(\frac{\lambda}{\lambda+\iota k}\right)^\alpha \tag{D.2}$$

On solving the above equation,

$$\begin{aligned}
\Phi(k) &= -\alpha\ln\left(1+\frac{ik}{\lambda}\right) \\
&= -\alpha\left[\left(\frac{ik}{\lambda}\right) - \frac{1}{2}\left(\frac{ik}{\lambda}\right)^2 + \frac{1}{3}\left(\frac{ik}{\lambda}\right)^3 + \dots\right] \\
&= \left[\frac{\alpha}{\lambda}(-\iota k) + \frac{\alpha}{\lambda^2}\frac{(-\iota k)^2}{2} + \frac{\alpha}{\lambda^3}\frac{(-\iota k)^3}{3} + \frac{\alpha}{\lambda^4}\frac{(-\iota k)^4}{4}\dots\right]
\end{aligned}$$

But $\Phi(k) = \ln(E[e^{-\iota kx}]) = E\left[\sum_{i=1}^\infty \frac{(-\iota kx)^n}{n!}\right]$ Writing term by term of these two results,

$$\begin{aligned}
&E\left[\frac{(-\iota kx)^0}{0!} + \frac{(-\iota kx)^1}{1!} + \frac{(-\iota kx)^2}{2!} + \frac{(-\iota kx)^4}{4!} + \dots\right] = \\
&\left[\frac{\alpha}{\lambda}(-\iota k) + \frac{\alpha}{\lambda^2}\frac{(-\iota k)^2}{2} + \frac{\alpha}{\lambda^3}\frac{(-\iota k)^3}{3} + \frac{\alpha}{\lambda^4}\frac{(-\iota k)^4}{4}\dots\right]
\end{aligned}$$

The r^{th} order cumulant, $E[x^r]$ is the coefficient of $(-\iota k)^r$, therefore comparing LHS and RHS we get,

$$\boxed{\begin{aligned} C_1 &= \frac{\alpha}{\lambda} \quad C_2 = \frac{\alpha}{\lambda^2} \\ C_3 &= \frac{2\alpha}{\lambda^3} \quad C_4 = \frac{6\alpha}{\lambda^4} \end{aligned}} \tag{D.3a}$$

Appendix E

Cumulant Error Analysis

The r^{th} moment static for a sample is defined as

$$m'_r = \frac{1}{n}\sum_{j=1}^{n} x_j^r \tag{E.1}$$

Th expectation value of rth moment is given as,

$$\begin{aligned} E[m'_r] &= \frac{1}{n}\sum_{j=1}^{n} E(x^r) \\ &= \frac{1}{n} n E(x^r) \\ &= \mu'_r \end{aligned} \tag{E.2}$$

By definition the variance is given as

$$Var(m'_r) = E\left(m'_r - E(m'_r)\right)^2 \tag{E.3}$$

On further simplifying the above equation,

$$\begin{aligned} Var(m'_r) &= E\left(\frac{1}{n}\sum_{j=1}^{n} x_j^r - \mu'_r\right)^2 \\ &= E\left(\left(\frac{1}{n}\sum x_j^r\right)^2 - \frac{2}{n}\mu'_r \sum x_j^r + (\mu'_r)^2\right) \\ &= \frac{1}{n^2}\left(E\left[\sum_{i=j} x_j^{2r} + \sum_{j\neq i}\sum x_i x_j - 2n\mu'_r \sum x_j^r + n^2(\mu'_r)^2\right]\right) \\ &= \frac{1}{n^2}\left(n\mu'_{2r} + n(n-1)(\mu'_r)^2 - n^2(\mu'_r)^2\right) \end{aligned}$$

Therefore,

$$\boxed{Var(m'_r) = \frac{1}{n}\left(\mu'_{2r} - (\mu'_r)^2\right)} \tag{E.4}$$

In this calculation x_i, x_j are assumed independent that's why the mean of the product and the product of the mean values are equal.

The covariance is defined as

$$\mathrm{Cov}(\mathrm{m}'_{\mathrm{q}}, \mathrm{m}'_{\mathrm{r}}) = \mathrm{E}\left(\mathrm{m}'_{\mathrm{q}} - \mu'_{\mathrm{q}}\right)\left(\mathrm{m}'_{\mathrm{r}} - \mu'_{\mathrm{r}}\right) \tag{E.5}$$

On simplification,

$$\begin{aligned}
\mathrm{Cov}(\mathrm{m}'_{\mathrm{q}}, \mathrm{m}'_{\mathrm{r}}) &= \mathrm{E}\left[\left(\frac{1}{\mathrm{n}}\sum \mathrm{x}_{\mathrm{q}} - \mu'_{\mathrm{q}}\right)\left(\frac{1}{\mathrm{n}}\sum \mathrm{x}_{\mathrm{r}} - \mu'_{\mathrm{r}}\right)\right] \\
&= \frac{1}{\mathrm{n}^2}\mathrm{E}\left[\sum \mathrm{x}^{\mathrm{q}}\sum \mathrm{x}^{\mathrm{r}} - \mathrm{n}\mu'_{\mathrm{r}}\sum \mathrm{x}^{\mathrm{q}} - \mathrm{n}\mu'_{\mathrm{q}} + \mathrm{n}^2\mu'_{\mathrm{q}}\mu'_{\mathrm{r}}\mathrm{n}^2\right] \\
&= \frac{1}{\mathrm{n}^2}\mathrm{E}\left[\sum_{\mathrm{i=j}} \mathrm{x}^{\mathrm{q+r}} + \sum_{\mathrm{i}\neq\mathrm{j}}\sum \mathrm{x}_{\mathrm{i}}^{\mathrm{q}}\mathrm{x}_{\mathrm{j}}^{\mathrm{r}}\right] - \frac{1}{\mathrm{n}}\left(\mu'_{\mathrm{q}}\mathrm{E}\left[\sum \mathrm{x}^{\mathrm{r}}\right] + \mu'_{\mathrm{r}}\mathrm{E}\left[\sum \mathrm{x}^{\mathrm{q}}\right]\right) + \mu'_{\mathrm{q}}\mu'_{\mathrm{r}} \\
&= \frac{\mu'_{q+r}}{n} + \frac{n-1}{n}\mu'_q\mu' r - \frac{2\mu'_q\mu' r}{n} + \mu'_q\mu'_r
\end{aligned}$$

Therefore,

$$\boxed{\mathrm{Cov}(\mathrm{m}'_{\mathrm{q}}, \mathrm{m}'_{\mathrm{r}}) = \frac{1}{\mathrm{n}}\left(\mu'_{\mathrm{q+r}} - \mu'_{\mathrm{q}}\mu'_{\mathrm{r}}\right)} \tag{E.6}$$

Now, the r^{th} central moment is defined as,

$$\mathrm{m}_{\mathrm{r}} = \frac{1}{\mathrm{n}}\sum_{j=1}^{n}\left(\mathrm{x}_j - \mathrm{m}'_1\right)^{\mathrm{r}} \tag{E.7}$$

here, $\mathrm{m}'_1 = \sum_{j=1}^{n} \mathrm{x}_j$ is the mean of the random variables x_j.

Now, the binomial expansion of the expectation value of m_{r} gives,

$$\begin{aligned}
\mathrm{E}(\mathrm{m}_{\mathrm{r}}) &= \mathrm{E}\left[\frac{1}{\mathrm{n}}\sum_{j=1}^{n}\left(\mathrm{x}_j - \mathrm{m}'_1\right)^{\mathrm{r}}\right] \\
&= \frac{1}{\mathrm{n}}\mathrm{E}\left[\sum_{j=1}^{n}\left({}^{\mathrm{r}}\mathrm{C}_0(\mathrm{x}_j)^{\mathrm{r}} + {}^{\mathrm{r}}\mathrm{C}_1(\mathrm{x}_j)^{\mathrm{r}-1}(-\mathrm{m}'_1)^1 + {}^{\mathrm{r}}\mathrm{C}_2(\mathrm{x}_j)^{\mathrm{r}-2}(-\mathrm{m}'_1)^2 + \ldots\right.\right. \\
&\left.\left. + {}^{\mathrm{r}}\mathrm{C}_r(\mathrm{x}_j)^0(-\mathrm{m}'_1)^r\right)\right]
\end{aligned} \tag{E.8}$$

Neglecting the terms which has $(\mathrm{m}_1)^{\mathrm{k}}$ for $\mathrm{k} > 2$ as $m_1 = f(1/\mathrm{n})$ and these terms will contribute less.

$$\mathrm{E}(\mathrm{m}_{\mathrm{r}}) = \frac{1}{\mathrm{n}}\mathrm{E}\left[\sum_{j=1}^{n}\left((\mathrm{x}_j)^{\mathrm{r}} + \mathrm{r}(\mathrm{x}_j)^{\mathrm{r}-1}(-\mathrm{m}'_1)^1 + \frac{\mathrm{r}(\mathrm{r}-1)}{2}(\mathrm{x}_j)^{\mathrm{r}-2}(-\mathrm{m}'_1)^2\right)\right] \tag{E.9}$$

Using the relation of m'$_1$ in the above equation,

$$\mathrm{E}(\mathrm{m_r}) = \frac{1}{\mathrm{n}}\mathrm{E}\left[\sum_{j=1}^{n}(\mathrm{x}_j)^{\mathrm{r}} - \frac{\mathrm{r}}{\mathrm{n}}\sum_{j=1}^{n}(\mathrm{x}_j)^{\mathrm{r}-1}\sum_{k=1}^{n}\mathrm{x}^k + \frac{\mathrm{r}(\mathrm{r}-1)}{2\mathrm{n}^2}\sum_{j=1}^{n}(\mathrm{x}_j)^{\mathrm{r}-2}\left(\sum_{k=1}^{n}\mathrm{x}^k\right)^2\right] \tag{E.10}$$

Each term in double summations are broken in view of random variable having same or different summation index.

$$\sum_{j=1}^{n}(\mathrm{x}_j)^{\mathrm{r}-1}\sum_{k=1}^{n}\mathrm{x}^k = \sum_{j=1}^{n}\mathrm{x}_j^{\mathrm{r}} + \sum_{\substack{j=1\\ j\neq k}}^{n}\sum_{k=1}^{n}\mathrm{x}_j^{\mathrm{r}-1}x_k$$

$$\sum_{j=1}^{n}(\mathrm{x}_j)^{\mathrm{r}-2}\sum_{k=1}^{n}\mathrm{x}^k\sum_{l=1}^{n}\mathrm{x}^l = \sum_{j=1}^{n}\mathrm{x}_j^{\mathrm{r}} + \sum_{\substack{j=1\\ j\neq(k=l)}}^{n}\sum_{k=1}^{n}\mathrm{x}_j^{\mathrm{r}-2}x_k^2 + \sum_{\substack{j=1\\ j\neq k\neq l)}}^{n}\sum_{k=1}^{n}\sum_{l=1}^{n}\mathrm{x}_j^{\mathrm{r}-2}x_k x_l$$

Applying in the inital eq.(E.10) so we finally get,

$$\mathrm{E}(\mathrm{m}^{\mathrm{r}}) = \frac{1}{\mathrm{n}}\mathrm{E}\left[\left(1 - \frac{\mathrm{r}}{\mathrm{n}} + \frac{\mathrm{r}(\mathrm{r}-1)}{2\mathrm{n}^2}\right)\sum\mathrm{x}_j^{\mathrm{r}} + \frac{\mathrm{r}(\mathrm{r}-1)}{2\mathrm{n}^2}\sum_{j\neq(k=l)}\sum\mathrm{x}_j^{\mathrm{r}-2}\mathrm{x}_k^2\right] \tag{E.12}$$

Note that the summation terms are devoid of index but it will be understood as before that each summation runs from 1 to n. Here few terms are missing as one might wonder, lets take one such term and find its expectation value,

$$\begin{aligned}
\mathrm{E}\left(\sum_{j\neq k}\sum\mathrm{x}_j^{\mathrm{r}-1}\mathrm{x}_k\right) &= \mathrm{E}\left(\sum\mathrm{x}_j^{\mathrm{r}-1}\right)\mathrm{E}\left(\sum\mathrm{x}_k\right)\\
&= \sum_{j\neq k}\sum\mathrm{E}[\mathrm{x}_j^{\mathrm{r}-1}]\mathrm{E}[\mathrm{x}_k]\\
&= \mathrm{n}(\mathrm{n}-1)\mu_{r-1}\mu_1 \quad \text{the factor comes from choosing i,j pair s.t. } \mathrm{i}\neq\mathrm{j}\\
&= 0 \qquad\qquad\qquad\qquad \text{as the first central moment } \mu_1 = 0
\end{aligned}$$

therefore terms with $\mathrm{E}\left(\sum x_a\right)$ will all contribute to zero. Again,

$$\mathrm{E}(\mathrm{m_r}) = \frac{1}{\mathrm{n}}\left[\left(1 - \frac{\mathrm{r}}{\mathrm{n}} + \frac{\mathrm{r}(\mathrm{r}-1)}{2\mathrm{n}^2}\right)(\mathrm{n}\mu_{\mathrm{r}}) + \mathrm{n}(\mathrm{n}-1)\frac{\mathrm{r}(\mathrm{r}-1)}{2\mathrm{n}^2}\mu_{\mathrm{r}-2}\mu_2\right]$$

for large n, terms with denominator n^k where $k \geq 2$ are ignored. Thus,

$$\boxed{E(m_r) = \left(1 - \frac{r}{n}\right)\mu_r + \frac{r(r-1)}{2n}\mu_{r-2}\mu_2} \tag{E.13}$$

To find the variance we need to find the $E[m_r^2]$. The calculations follow the same pattern as above,

$$\begin{aligned}
E(m_r^2) &= \frac{1}{n^2}E\left[\left\{\sum (x_j - m_1')^r\right\}^2\right] \\
&= \frac{1}{n^2}E\left[\left\{\sum x_j^r - \frac{r}{n}\sum x_j^{r-1}\sum x_k + \frac{r(r-1)}{2n^2}\sum x_j^{r-2}\left(\sum x_k\right)^2\right\}^2\right] \\
&= \frac{1}{n^2}E\left[\left(\sum x_j^{r-2}\right)^2 + \frac{r^2}{n^2}\left(\sum x_j^{r-1}\sum x_k\right)^2 + \left(\frac{r(r-1)}{2n^2}\right)^2\left(\sum x^{r-2}\left(\sum x_k\right)^2\right)^2\right. \\
&\quad - \frac{2r}{n}\sum x_j^r\sum x_k^{r-1}\sum x_l - \frac{r(r-1)}{n^2}\sum x_j^r\sum x_k^{r-2}\left(\sum x_l\right)^2 \\
&\quad \left. - \frac{r^2(r-1)}{n^3}\sum x_j^{r-1}\sum x_k^{r-2}(x_l)^2\right]
\end{aligned} \tag{E.14}$$

Now term by term analysis of RHS of eq.(E.14) is done to get the results.

The first term,

$$\begin{aligned}
E\left[\left(\sum x_j^r\right)^2\right] &= E\left[\sum x_j^{2r} + \sum_{j\neq k}\sum x_j^r x_k^r\right] \\
&= n\mu_{2r} + n(n-1)\mu_r^2
\end{aligned} \tag{E.15}$$

The second term,

$$
\begin{aligned}
&\mathrm{E}\left[\left(\sum \mathrm{x}_\mathrm{j}^{\mathrm{r}-1}\sum \mathrm{x}_\mathrm{k}\right)^2\right] = \mathrm{E}\left[\sum \mathrm{x}_\mathrm{j}^{\mathrm{r}-1}\sum \mathrm{x}_\mathrm{k}\sum \mathrm{x}_\mathrm{m}^{\mathrm{r}-1}\sum \mathrm{x}_\mathrm{n}\right] \\
&= \mathrm{E}\Bigg[\sum \mathrm{x}_\mathrm{j}^{2\mathrm{r}} + \sum_{\text{onlyj=k}} \mathrm{x}_\mathrm{j}^{\mathrm{r}-1}\sum \mathrm{x}_\mathrm{m}^{\mathrm{r}-1}\cancelto{0}{\textstyle\sum x_n} + \sum_{\text{onlyj=m}} \mathrm{x}_\mathrm{j}^{2(\mathrm{r}-1)}\sum \mathrm{x}_\mathrm{k}\cancelto{0}{\textstyle\sum x_n} \\
&+ \sum_{\text{onlyj=n}} \mathrm{x}_\mathrm{j}^{\mathrm{r}}\sum \mathrm{x}_\mathrm{m}^{\mathrm{r}-1}\cancelto{0}{\textstyle\sum x_k} + \sum_{\mathrm{j=k=m}} \mathrm{x}_\mathrm{j}^{2(\mathrm{r}-1)+1}\cancelto{0}{\textstyle\sum x_n} + \sum_{\mathrm{j=m=n}} \mathrm{x}_\mathrm{j}^{2(\mathrm{r}-1)+1}\cancelto{0}{\textstyle\sum x_k} \\
&+ \sum_{\mathrm{j=k=n}} \mathrm{x}_\mathrm{j}^{\mathrm{r}+1}\sum \mathrm{x}_\mathrm{m}^{\mathrm{r}-1} + \sum \mathrm{x}_\mathrm{j}^{\mathrm{r}-1}\sum_{\mathrm{k=m}} \mathrm{x}_\mathrm{m}^{\mathrm{r}}\cancelto{0}{\textstyle\sum x_n} + \sum \mathrm{x}_\mathrm{j}^{\mathrm{r}-1}\cancelto{0}{\textstyle\sum x_k}\sum_{\mathrm{m=n}} \mathrm{x}_\mathrm{m}^{\mathrm{r}} \\
&+ \sum \mathrm{x}_\mathrm{j}^{\mathrm{r}-1}\sum \mathrm{x}_\mathrm{m}^{\mathrm{r}-1}\sum_{\mathrm{k=n}} \mathrm{x}_\mathrm{k}^{2} + \sum\sum\sum\sum_{\mathrm{j\neq k\neq m\neq n}} \mathrm{x}_\mathrm{j}^{\mathrm{r}-1}\mathrm{x}_\mathrm{k}\mathrm{x}_\mathrm{n}^{\mathrm{r}-1}\cancelto{0}{\textstyle\sum x_n}\Bigg] \\
&= \mathrm{E}\left[\sum_{\mathrm{j=k=m=n}} \mathrm{x}_\mathrm{j}^{2\mathrm{r}} + \sum_{\mathrm{j=k=n}} \mathrm{x}_\mathrm{j}^{\mathrm{r}+1}\sum \mathrm{x}_\mathrm{m}^{\mathrm{r}-1} + \sum \mathrm{x}_\mathrm{j}^{\mathrm{r}-1}\sum_{\mathrm{k=n}} \mathrm{x}_\mathrm{k}^{2}\sum \mathrm{x}_\mathrm{m}^{\mathrm{r}-1}\right] \\
&= \mathrm{n}\mu_{2\mathrm{r}} + \mathrm{n}(\mathrm{n}-1)\mu_{\mathrm{r}+1}\mu_{\mathrm{r}-1} + \mathrm{n}(\mathrm{n}-1)(\mathrm{n}-2)\mu_{\mathrm{r}-1}^2 + \mu^2
\end{aligned}
\tag{E.16}
$$

The third and sixth terms in RHS of eq.(E.14) have coefficients of $1/\mathrm{n}^4$ and $1/\mathrm{n}^3$ respectively and they tends to zero for large value of n. Thus are neglected.

The forth term,

$$
\begin{aligned}
\mathrm{E}\left[\sum \mathrm{x}_\mathrm{j}^{\mathrm{r}}\sum \mathrm{x}_\mathrm{k}^{\mathrm{r}-1}\sum \mathrm{x}_\mathrm{l}\right] &= \mathrm{E}\Bigg[\sum_{\mathrm{j=k=l}} \mathrm{x}_\mathrm{j}^{2\mathrm{r}} + \sum_{\mathrm{j=k\neq l}} \mathrm{x}_\mathrm{j}^{2\mathrm{r}-1}\cancelto{0}{\textstyle\sum x_l} \\
&\quad + \sum_{\mathrm{k=l\neq j}} \mathrm{x}_\mathrm{k}^{\mathrm{r}}\sum \mathrm{x}_\mathrm{j}^{\mathrm{r}} + \sum_{\mathrm{j=l\neq k}} \mathrm{x}_\mathrm{j}^{\mathrm{r}+1}\sum \mathrm{x}_\mathrm{k}^{\mathrm{r}-1}\Bigg] \\
&= \mathrm{n}\mu_{2\mathrm{r}} + \mathrm{n}(\mathrm{n}-1)\mu_\mathrm{r}^2 + \mathrm{n}(\mathrm{n}-1)\mu_{\mathrm{r}+1}\mu_{\mathrm{r}-1}
\end{aligned}
\tag{E.17}
$$

The fifth term,

$$
\begin{aligned}
&\mathrm{E}\left[\sum \mathrm{x}_\mathrm{j}^{\mathrm{r}}\sum \mathrm{x}_\mathrm{k}^{\mathrm{r}-2}\left(\sum \mathrm{x}_\mathrm{l}\right)^2\right] = \left[\sum \mathrm{x}_\mathrm{j}^{\mathrm{r}}\sum \mathrm{x}_\mathrm{k}^{\mathrm{r}-2}\left(\sum \mathrm{x}_\mathrm{l}^2 + \sum_{\mathrm{l\neq m}} \mathrm{x}_\mathrm{l}\sum \mathrm{x}_\mathrm{m}\right)\right] \\
&= \mathrm{E}\left[\sum \mathrm{x}_\mathrm{j}^{\mathrm{r}}\sum \mathrm{x}_\mathrm{k}^{\mathrm{r}-2}\sum \mathrm{x}_\mathrm{l}^2\right] + \mathrm{E}\left[\sum \mathrm{x}_\mathrm{j}^{\mathrm{r}}\sum \mathrm{x}_\mathrm{k}^{\mathrm{r}-2}\cancelto{0}{\sum_{l\neq m} x_l}\sum \mathrm{x}_\mathrm{m}\right] \\
&= \mathrm{n}(\mathrm{n}-1)(\mathrm{n}-2)\mu_\mathrm{r}\mu_{\mathrm{r}-2}\mu_2
\end{aligned}
\tag{E.18}
$$

Therefore, taking the results (E.15), (E.16, (E.17) & (E.18) and using in eq. (E.14),

$$\mathrm{E}\left[\mathrm{m}_\mathrm{r}^2\right] = \frac{1}{\mathrm{n}^2}\left[\left(\mathrm{n}\mu_{2\mathrm{r}} + \mathrm{n}(\mathrm{n}-1)\mu_\mathrm{r}^2\right) + \frac{\mathrm{r}^2}{\mathrm{n}^2}\left(\mathrm{n}\mu_{2\mathrm{r}} + \mathrm{n}(\mathrm{n}-1)\mu_{\mathrm{r}+1}\mu_{\mathrm{r}-1} + \mathrm{n}(\mathrm{n}-1)(\mathrm{n}-2)\mu_{\mathrm{r}-1}^2 + \mu^2\right)\right.$$
$$\left. -\frac{2\mathrm{r}}{\mathrm{n}}\left(\mathrm{n}\mu_{2\mathrm{r}} + \mathrm{n}(\mathrm{n}-1)\mu_\mathrm{r}^2 + \mathrm{n}(\mathrm{n}-1)\mu_{\mathrm{r}+1}\mu_{\mathrm{r}-1}\right) - \frac{\mathrm{r}(\mathrm{r}-1)}{\mathrm{n}^2}\,()\right] \tag{E.19}$$

Now, terms having terms $\mathrm{f}(1/\mathrm{n}^k)$ for $\mathrm{k} \geq 2$ are neglected assuming large value of n. Therefore,

$$\boxed{\mathrm{E}\left[\mathrm{m}_\mathrm{r}^2\right] = \frac{1}{\mathrm{n}}\left(\mu_{2\mathrm{r}} + (\mathrm{n}-1)\mu_\mathrm{r}^2 + \mathrm{r}^2\mu_{\mathrm{r}-1}^2\mu_2 - 2\mathrm{r}(\mu_{\mathrm{r}+1}\mu_{\mathrm{r}-1} + \mu_\mathrm{r}^2) + \mathrm{r}(\mathrm{r}-1)\mu_\mathrm{r}\mu_{\mathrm{r}-2}\mu_2\right)} \tag{E.20}$$

The variance is given as,

$$\begin{aligned}
\mathrm{Var}(\mathrm{m}_\mathrm{r}) &= \mathrm{E}[\mathrm{m}_\mathrm{r}^2] - (\mathrm{E}[\mathrm{m}_\mathrm{r}])^2 \\
&= \mathrm{E}[\mathrm{m}_\mathrm{r}^2] - \left(\left(1 - \frac{2\mathrm{r}}{\mathrm{n}}\right)\mu_\mathrm{r}^2 + \frac{\mathrm{r}(\mathrm{r}-1)}{\mathrm{n}}\mu_\mathrm{r}\mu_{\mathrm{r}-2}\mu_2\right) \\
&= \frac{1}{\mathrm{n}}\left\{\left(\mu_{2\mathrm{r}} + (\mathrm{n}-1)\mu_\mathrm{r}^2 + \mathrm{r}^2\mu_{\mathrm{r}-1}^2\mu_2 - 2\mathrm{r}(\mu_{\mathrm{r}+1}\mu_{\mathrm{r}-1} + \mu_\mathrm{r}^2) + \mathrm{r}(\mathrm{r}-1)\mu_\mathrm{r}\mu_{\mathrm{r}-2}\mu_2\right)\right. \\
&\qquad \left. -(\mathrm{n}-2\mathrm{r})\mu_\mathrm{r}^2 - \mathrm{r}(\mathrm{r}-1)\mu_\mathrm{r}\mu_{\mathrm{r}-2}\mu_2\right\}
\end{aligned} \tag{E.21}$$

Again if someone notices the terms of $\mathrm{O}(1/\mathrm{n}^2)$ are neglected as for large value of n these tends to zero. **Finally** the variance of the r^{th} central moment is given as,

$$\boxed{\mathrm{Var}(\mathrm{m}_\mathrm{r}) = \frac{1}{\mathrm{n}}\left[\mu_{2\mathrm{r}} - \mu_\mathrm{r}^2 + \mathrm{r}^2\mu_{\mathrm{r}-1}^2\mu_2 - 2\mathrm{r}\mu_{\mathrm{r}+1}\mu_{\mathrm{r}-1}\right]} \tag{E.22}$$

If we compare the equation of Variance (E.4) to Covariance (E.6) equation is obtained through these simple relationships $2\mathrm{r} \longrightarrow \mathrm{r}+\mathrm{q}$, $(\mu_\mathrm{r}')^2 \longrightarrow \mu_\mathrm{r}'\mu_\mathrm{q}'$ & $\mathrm{r}^2 \longrightarrow rq$.

The rigorous calculation is ignored in this phase and with these simple relations we get the final equation of Covariance for a central moment as follows :

$$\boxed{\mathrm{Cov}\left(\mathrm{m}_\mathrm{r}, \mathrm{m}_\mathrm{q}\right) = \frac{1}{\mathrm{n}}\left[\mu_{\mathrm{r}+\mathrm{q}} - \mu_\mathrm{r}\mu_\mathrm{q} + \mathrm{rq}\mu_{\mathrm{r}-1}\mu_{\mathrm{q}-1}\mu_2 - \mathrm{r}\mu_{\mathrm{r}-1}\mu_{\mathrm{q}+1} - \mathrm{q}\mu_{\mathrm{r}+1}\mu_{\mathrm{q}-1}\right]} \tag{E.23}$$

Let use assume a function of k random variables to be $g(x) = g(x_1, x_2, x_3, \ldots, x_k)$ and the mean of each random variable is $\theta_1, \theta_2, \theta_3, \ldots, \theta_k$ respectively. On Taylor expansion of g(x) up untill two terms,

$$g(x) = g(\theta) + \sum_{i=1}^{k} g^{'}(\theta_i)(x_i - \theta_i)$$

here, $g^{'}(\theta_i) = \left|\frac{\partial g}{\partial x_i}\right|_{x_i=\theta_i}$. The expectation value of g(x) will be

$$\begin{aligned} E\left[g(x)\right] &= E\left[g(\theta)\right] + \cancelto{0}{\sum_{i=1}^{k} g^{'}(\theta_i) E\left[(x_i - \theta_i)\right]} \\ &= g(\theta) \end{aligned}$$

and the Variance of g(x) will be

$$\begin{aligned} Var(g(x)) &= E\left[\sum g'(\theta_i)(x_i - \theta_i)\right]^2 \\ &= \sum E[g'(\theta_i)^2] E\left[x_i - \theta_i\right]^2 + \sum_{i \neq j} \sum E[g'(\theta_i) g'(\theta_j)] E\left[(x_i - \theta_i)(x_j - \theta_j)\right] \end{aligned}$$

Using the definition of variance and covariance as done before the variance of g(x) comes out to be,

$$\boxed{Var(g(x)) = \sum E[g'(\theta_i)^2] Var(x_i) + \sum_{i \neq j} \sum E[g'(\theta_i) g'(\theta_j)] Cov(x_i, x_j)} \tag{E.24}$$

The relation between the first four cumulants and moments are

$$C_1 = m_1' \tag{E.25}$$

$$C_2 = m_2 \tag{E.26}$$

$$C_3 = m_3 \tag{E.27}$$

$$C_4 = m_4 - 3m_2^2 \tag{E.28}$$

The Variance on the first three cumulant can be written down directly from the relations (E.4) and (E.22) and they are,

$$\mathrm{Var}(C_1) = \mathrm{Var}(m_1') = \frac{1}{n}\left[\ \mu_2' - (\mu_1')^2\ \right] = \frac{\mu_2}{n}$$
$$\mathrm{Var}(C_2) = \mathrm{Var}(m_2) = \frac{1}{n}\left[\ \mu_4 - \mu_2^2 + 4\mu_1^2\mu_2 \xrightarrow{0} - 4\mu_3\mu_1 \xrightarrow{0}\right] = \frac{1}{n}\left[\mu_4 - \mu_2^2\right]$$
$$\mathrm{Var}(C_3) = \mathrm{Var}(m_3) = \frac{1}{n}\left[\ \mu_6 - \mu_3^2 + 9\mu_2^3 - 6\mu_4\mu_2\ \right]$$

The Variance of C_4 can be obtained using eq.(E.24). Let assume $c_4 = g(m_4, m_2)$ and the expectation value of m_4, m_2 is μ_4, μ_2 respectively. Therefore the variance is ,

$$\begin{aligned}\mathrm{Var}(C_4) = \mathrm{Var}(g(m_4, m_2)) &= E\left[\left(\frac{\partial g}{\partial m_4}\right)^2 (m_4 - \mu_4)^2 + \left(\frac{\partial g}{\partial m_2}\right)^2 (m_2 - \mu_2)^2\right.\\ &\left. + \left(\frac{\partial g}{\partial m_4}\frac{\partial g}{\partial m_2}\right)(m_4 - \mu_4)(m_2 - \mu_2) + \left(\frac{\partial g}{\partial m_2}\frac{\partial g}{\partial m_4}\right)(m_4 - \mu_4)(m_2 - \mu_2)\right]\\ &= \mathrm{Var}(m_4) + 36\mu_2^2\mathrm{Var}(m_2) - 12\mu_2\mathrm{Cov}(m_4, m2)\\ &= \frac{1}{n}\left[\ \mu_8 - 12\mu_6\mu_2 - 8\mu_5\mu_3 - \mu_4^2 + 48\mu_4\mu_2^2 + 64\mu_3^2\mu_2 - 36\mu_2^4\ \right]\end{aligned}$$

Hence the variance in cumulants are,

$$\mathrm{Var}(C_1) = \frac{\mu_2}{n} \tag{E.29a}$$
$$\mathrm{Var}(C_2) = \frac{1}{n}\left[\mu_4 - \mu_2^2\right] \tag{E.29b}$$
$$\mathrm{Var}(C_3) = \frac{1}{n}\left[\ \mu_6 - \mu_3^2 + 9\mu_2^3 - 6\mu_4\mu_2\ \right] \tag{E.29c}$$
$$\mathrm{Var}(C_4) = \frac{1}{n}\left[\ \mu_8 - 12\mu_6\mu_2 - 8\mu_5\mu_3 - \mu_4^2 + 48\mu_4\mu_2^2 + 64\mu_3^2\mu_2 - 36\mu_2^4\ \right] \tag{E.29d}$$

The results have been verified from the book “Kendall’s Advanced Theory of Statistics. Volume 1. Distribution Theory " [35].

Appendix F

χ^2/ndf test for goodness-of-fit

Let us consider N to be no of bins in a histogram and M_i to be the no. of measured events in bins. Usually, M_i follows the Poisson's distribution $f(M_i;\theta)$, here $\theta(\theta_1, \theta_2, \theta_3 \ldots \theta_n)$ are n unknown parameters. The expectation value of M_i, E[M_i] assuming Poisson distribution is $\mu_1(\theta_i)$ or simply for notation, μ_i.

The likelihood function is a joint probability density function (p.d.f.) for the data is given as

$$\mathrm{L}(\mu(\theta);\mathrm{M}) = \prod_{i-1}^{N} \frac{e^{\mu_i}\mu_i^{M_i}}{M_i} \tag{F.1}$$

The maximum likelihood estimator (MLE) of θ can be constructed by maximizing the likelihood ratio $\lambda(\theta)$

$$\lambda(\theta) = \frac{\mathrm{L}(\mu(\theta);\mathrm{M}}{\max\{\mathrm{L}(\hat{\mu};\mathrm{M})\}}$$

This is equivalent to just maximizing the likelihood function. The maximum of likelihood function, $\mathrm{L}(\hat{\mu_\mathrm{i}};\mathrm{M})$ can be found by solving the differential equations (generally any one function of the product term gives the estimator)

$$\left.\frac{\partial \mathrm{L}}{\partial \mu_\mathrm{i}}\right|_{\mu_\mathrm{i}=\hat{\mathrm{mu}}_\mathrm{i}} = 0 \quad \text{for any value of i } = 1, 2, 3, \ldots, n \tag{F.2}$$

It is also equivalent to minimizing the corresponding χ^2 function defined as

$$\chi^2 = -2\ln\lambda(\theta) \tag{F.3}$$

For large no. of data points in each bin, Poisson distribution approaches or say is approximated as Gaussian distribution with,

$$\mathrm{E}[\mathrm{M_i}] = \mu_\mathrm{i}(\theta) \tag{F.4}$$

$$\mathrm{Var}(\mathrm{M_i}) = \sigma_\mathrm{i}^2 = \mu_\mathrm{i}(\theta) \tag{F.5}$$

Now the likelihood function is given as,

$$L_{Gauss}\left(\mu(\theta); M\right) = \prod_{i=1}^{N} \frac{1}{\sqrt{2\pi\mu_i(\theta)}} \exp\left(-\frac{(\mu_i(\theta) - M_i)^2}{2\mu_i(\theta)}\right) \tag{F.6}$$

Lets find $\hat{\mu}_i$ for a arbitrary bin,

$$\begin{aligned}
\frac{\partial L}{\partial \mu} &= \frac{\partial}{\partial \mu}\left[\frac{1}{\sqrt{2\pi\mu}} \exp\left(-\frac{(\mu - M)^2}{2\mu}\right)\right] \\
&= \frac{1}{\sqrt{2\pi\mu}} \exp\left(-\frac{(\mu - M)^2}{2\mu}\right)\left[-\frac{1}{2\mu} - \left\{\frac{2\mu(\mu - M) - (\mu - M)^2}{2\mu^2}\right\}\right] \\
&= \frac{1}{\sqrt{2\pi\mu}} \exp\left(-\frac{(\mu - M)^2}{2\mu}\right)\left[-\frac{1}{2\mu}\left\{\mu^2 + \mu - M^2\right\}\right]
\end{aligned}$$

For $\mu \neq 0$ and $\mu \neq \infty$, $\left.\frac{\partial L}{\partial \mu}\right|_{\mu=\hat{\mu}} = 0$ can be obtained by solving the quadratic equation $\mu^2 + \mu - M^2$. The two values are, $\sqrt{1/4 + M} - 1/2$ and $-\sqrt{1/4 + M} - 1/2$. The negative value is neglected as on using this value in the factor $\frac{1}{\sqrt{2\pi\mu}}$ it makes function imaginary. But the former value is positive always and hence also the Gaussian function. A positive μ valued Gaussian function is always positive and has one peak at mean, μ. Therefore, for $\hat{\mu} = \sqrt{1/4 + M} - 1/2$ the likelihood function is maximum.

The Gaussian-χ^2 can be written using eq. (F) as,

$$\begin{aligned}
\chi^2_{Gauss} &= -2\ln\lambda_{Gauss}(\theta) \\
&= -2\ln\left[\frac{L_{Gauss}(\mu; M)}{\max\left\{L_{Gauss}(\hat{\mu}; M)\right\}}\right] \\
&= -2\ln\left[\frac{L_{Gauss}(\mu; M)}{L_{Gauss}(\hat{\mu}; M)}\right] \\
&= -2\sum_{i=1}^{N}\left[\ln\left(\frac{1}{\sqrt{2\pi\mu_i}}\right) - \frac{(\mu_i - M_i)^2}{2\mu_i} - \ln\left(\frac{1}{\sqrt{2\pi\hat{\mu}_i}}\right) + \frac{(\hat{\mu}_i - M_i)^2}{2\hat{\mu}_i}\right] \\
&= \sum_{i=1}^{N}\left[\frac{(\mu_i - M_i)^2}{\mu_i} + \ln\left(\frac{\mu_i}{\hat{\mu}_i}\right) - \frac{(\hat{\mu}_i - M_i)^2}{\hat{\mu}_i}\right]
\end{aligned}$$

Now, for large statistics, $M_i \to \infty$ implying $\hat{\mu}_i \to \infty$. Thus, $\hat{\mu}_i \approx M_i$. This condition simplifies the upper result by following two approximation,

$$(\hat{\mu}_i - M_i) \approx 0 \approx \frac{(\hat{\mu}_i - M_i)^2}{\hat{\mu}_i}$$

$\ln\left(\frac{\mu}{\hat{\mu}}\right) \approx \ln\left(\frac{\mu_i}{M_i}\right) \approx \ln(1)(=0)$ for large statistics, model and observed mean are comparable Therefore,

$$\boxed{\chi^2_{\text{Gauss}} = \sum_{i=1}^{N} \frac{(\mu_i(\theta) - M_i)^2}{\mu_i(\theta)}} \tag{F.7}$$

This χ^2 formula is widely known as χ^2_{Pearson}. The χ^2 distribution is given by,

$$P_r(x) = \frac{x^{\frac{r}{2}-1} e^{-\frac{x}{2}}}{\Gamma(\frac{r}{2}) 2^{\frac{r}{2}}} \tag{F.8}$$

Here, $x = \chi^2$ value and r is the no. of degrees of freedom (no. of data points - no. of parameter of the fitting model). If we compare the above eq.(F.8) with Gamma distribution (**??**) then it is clear that χ^2 distribution is a Gamma distribution with Gamma parameter $(\alpha, \lambda) = (\frac{r}{2}, \frac{1}{2})$. Therefore using the relations (D.3a), the mean of the Gamma distribution is given as $C_1 = \frac{\alpha}{\lambda} = \frac{r/2}{1/2} = r$. Therefore, for good fit one expects that $\chi^2 \approx r$ or $\chi^2/\text{ndf} \approx 1$ [36, 37].

Bibliography

[1] M. M. Aggarwal et al. "Event-by-event fluctuations in particle multiplicities and transverse energy produced in 158-A-GeV Pb + Pb collisions". In: *Phys. Rev. C* 65 (2002), p. 054912. DOI: 10.1103/PhysRevC.65.054912. arXiv: nucl-ex/0108029.

[2] M.J. Tannenbaum. "The distribution function of the event-by-event average pT for statistically independent emission". In: *Physics Letters B* 498.1 (2001), pp. 29–34. ISSN: 0370-2693.

[3] Tom W.B. Kibble. "The Standard Model of Particle Physics". In: *European Review* 23.1 (2015), pp. 36–44. DOI: 10.1017/S1062798714000520.

[4] ALICE collaboration. "https://alice-collaboration.web.cern.ch/". In: ().

[5] David J. Gross and Frank Wilczek. "Asymptotically Free Gauge Theories. I". In: *Phys. Rev. D* 8 (10 Nov. 1973), pp. 3633–3652. DOI: 10.1103/PhysRevD.8.3633. URL: https://link.aps.org/doi/10.1103/PhysRevD.8.3633.

[6] David J. Gross and Frank Wilczek. "Asymptotically free gauge theories. II". In: *Phys. Rev. D* 9 (4 Feb. 1974), pp. 980–993. DOI: 10.1103/PhysRevD.9.980. URL: https://link.aps.org/doi/10.1103/PhysRevD.9.980.

[7] Ulrich Heinz et al. "Exploring the properties of the phases of QCD matter - research opportunities and priorities for the next decade". In: (Jan. 2015). arXiv: 1501.06477 [nucl-th].

[8] Y Aoki et al. "The order of the quantum chromodynamics transition predicted by the standard model of particle physics". In: *Nature* 443.hep-lat/0611014 (Nov. 2006), 675–678. 7 p. URL: https://cds.cern.ch/record/998395.

[9] Tanmoy Bhattacharya et al. "QCD Phase Transition with Chiral Quarks and Physical Quark Masses". In: *Phys. Rev. Lett.* 113 (8 Aug. 2014), p. 082001. DOI: 10.1103/PhysRevLett.113.082001. URL: https://link.aps.org/doi/10.1103/PhysRevLett.113.082001.

[10] J. C. Collins and M. J. Perry. "Superdense Matter: Neutrons or Asymptotically Free Quarks?" In: *Phys. Rev. Lett.* 34 (21 May 1975), pp. 1353–1356. DOI: 10.1103/PhysRevLett.34.1353. URL: https://link.aps.org/doi/10.1103/PhysRevLett.34.1353.

[11] "Centrality determination in heavy ion collisions". In: (Aug. 2018). URL: https://cds.cern.ch/record/2636623.

[12] Dmitri Kharzeev and Marzia Nardi. "Hadron production in nuclear collisions at RHIC and high density QCD". In: *Phys. Lett. B* 507 (2001), pp. 121–128. DOI: 10.1016/S0370-2693(01)00457-9. arXiv: nucl-th/0012025.

[13] Stefan Heckel and. "Event-by-event meanpTfluctuations in pp and Pb–Pb collisions measured by the ALICE experiment at the LHC". In: *Journal of Physics G: Nuclear and Particle Physics* 38.12 (Nov. 2011), p. 124095. DOI: 10.1088/0954-3899/38/12/124095. URL: https://doi.org/10.1088/0954-3899/38/12/124095.

[14] Gordon Baym and Henning Heiselberg. "Event-by-event fluctuations in ultrarelativistic heavy-ion collisions". In: *Physics Letters B* 469.1 (1999), pp. 7–11. ISSN: 0370-2693. DOI: https://doi.org/10.1016/S0370-2693(99)01263-0. URL: https://www.sciencedirect.com/science/article/pii/S0370269399012630.

[15] Torbjörn Sjöstrand et al. "An introduction to PYTHIA 8.2". In: *Comput. Phys. Commun.* 191 (2015), pp. 159–177. DOI: 10.1016/j.cpc.2015.01.024. arXiv: 1410.3012 [hep-ph].

[16] Jesper Roy Christiansen. *Colour Reconnection and Weak Showers*. Defence details Date: 2015-11-13 Time: 13:00 Place: Lundmarksalen, Sölvegatan 27, Lund External reviewer(s) Name: Gieseke, Stefan Affiliation: Karlsruhe Institute of Technology —. 2015.

[17] A. Ortiz Velasquez et al. "Color Reconnection and Flowlike Patterns in pp Collisions". In: *Phys. Rev. Lett.* 111 (4 July 2013), p. 042001. DOI: 10.1103/PhysRevLett.111.042001.

[18] Jaroslav Adam et al. "Enhanced production of multi-strange hadrons in high-multiplicity proton-proton collisions". In: *Nature Phys.* 13 (2017), pp. 535–539. DOI: 10.1038/nphys4111. arXiv: 1606.07424 [nucl-ex].

[19] Gosta Gustafson. "Multiple Interactions, Saturation, and Final States in pp Collisions and DIS". In: *Acta Phys. Polon. B* 40 (2009). Ed. by Krzysztof Golec-Biernat and Michal Praszalowicz, pp. 1981–1996. arXiv: 0905.2492 [hep-ph].

[20] Christian Bierlich, Gösta Gustafson, and Leif Lönnblad. "A shoving model for collectivity in hadronic collisions". In: (Dec. 2016). arXiv: 1612.05132 [hep-ph].

[21] The Collaboration et al. "The alice experiment at the CERN LHC". In: *Journal of Instrumentation* 3 (Aug. 2008), S08002. DOI: 10.1088/1748-0221/3/08/S08002.

[22] Cinzia De Melis. "The CERN accelerator complex. Complexe des accélérateurs du CERN". In: (Jan. 2016). General Photo. URL: https://cds.cern.ch/record/2119882.

[23] Sourav Kundu. "Angular and momentum distribution of vector mesons produced in proton-proton and heavy-ion collisions at LHC energies". Oct. 2020. URL: https://cds.cern.ch/record/2751550.

[24] Subhash Singha. "Identified particle production in Pb-Pb and pp collisions at LHC energies". PhD thesis. Bhubaneswar, NISER, Sept. 2014.

[25] Domenico Colella. "ALICE ITS: the Run 1 to Run 2 transition and recent operational experience". In: *PoS* (2015), p. 003.

[26] Alexander Kalweit. "Production of light flavor hadrons and anti-nuclei at the LHC". 2012. URL: https://cds.cern.ch/record/2119440.

[27] Steffen Georg Weber and Anton Andronic. "ALICE event display of a Pb-Pb collision at 5.02A TeV". General Photo. July 2016. URL: https://cds.cern.ch/record/2202730.

[28] ALICE. *The ALICE Time of Flight Detector*. URL: http://aliweb.cern.ch/public/en/Chapter2/Chap2_TOF.html (visited on 07/05/2021).

[29] Stefan Schmitt and Daniel Britzger. *Unfolding in High Energy Physics*. Ed. by Stefan Schmitt. URL: https://www.desy.de/~sschmitt/talks/UnfoldStatSchool2014.pdf.

[30] Tim Adye. *Unfolding algorithms and tests using RooUnfold*. 2011. arXiv: 1105.1160.

[31] Betty Bezverkhny Abelev et al. "Multiplicity dependence of the average transverse momentum in pp, p-Pb, and Pb-Pb collisions at the LHC". In: *Phys. Lett. B* 727 (2013), pp. 371–380. DOI: 10.1016/j.physletb.2013.10.054. arXiv: 1307.1094 [nucl-ex].

[32] Xiaofeng Luo et al. "Volume fluctuation and auto-correlation effects in the moment analysis of net-proton multiplicity distributions in heavy-ion collisions". In: *Journal of Physics G: Nuclear and Particle Physics* 40.10 (Sept. 2013), p. 105104. DOI: 10.1088/0954-3899/40/10/105104. URL: https://doi.org/10.1088/0954-3899/40/10/105104.

[33] Cheuk-Yin Wong. *Introduction to High-Energy Heavy-Ion Collisions*. WORLD SCIENTIFIC, 1994. DOI: 10.1142/1128. eprint: https://www.worldscientific.com/doi/pdf/10.1142/1128. URL: https://www.worldscientific.com/doi/abs/10.1142/1128.

[34] G. D'Agostini. "A multidimensional unfolding method based on Bayes' theorem". In: *Nuclear Instruments and Methods in Physics Research Section A: Accelerators, Spectrometers, Detectors and Associated Equipment* 362.2 (1995), pp. 487–498. ISSN: 0168-9002. DOI: https://doi.org/10.1016/0168-9002(95)00274-X.

[35] P. Davies. "Kendall's Advanced Theory of Statistics. Volume 1. Distribution Theory". In: *Journal of the Royal Statistical Society Series A* 151.1 (Jan. 1988), pp. 240–240. DOI: 10.2307/2982217. URL: https://ideas.repec.org/a/bla/jorssa/v151y1988i1p240-240.html.

[36] Cowan Glen. *Introduction to Statistical Methods 2011 CERN Summer Student Lectures*. 2011. URL: http://www.pp.rhul.ac.uk/~cowan/stat/cern/cern_stat_4.pdf.

[37] Cowan Glen, F. James, and R. Cousins. *Statistics*. 2005. URL: https://pdg.lbl.gov/2006/reviews/statrpp.pdf.